Mon. Not. R. Astron. Soc. **374,** 703–720 (2007) doi:10.1111/j.1365-2966.2006.11184.x

A comprehensive NBODY study of mass segregation in star clusters: energy equipartition and escape

E. Khalisi,[1⋆] P. Amaro-Seoane[2⋆] and R. Spurzem[1⋆]

[1]*Astronomisches Rechen-Institut, Mönchhofstraße 12-14, Heidelberg, D-69120, Germany*
[2]*Am Muehlenberg 1, D-14476 Potsdam, Germany*

Accepted 2006 October 9. Received 2006 September 23

ABSTRACT

We address the dynamical evolution of an isolated self-gravitating system with two stellar mass groups. We vary the individual ratio of the heavy to light bodies, μ from 1.25 to 50 and alter also the fraction of the total heavy mass $\mathcal{M}_{\rm h}$ from 5 to 40 per cent of the whole cluster mass. Clean-cut properties of the cluster dynamics are examined, like core collapse, the evolution of the central potential, as well as escapers. We present in this work collisional *N*-body simulations, using the high-order integrator NBODY6++ with up to $\mathcal{N}_\star = 2 \times 10^4$ particles improving the statistical significancy of the lower-$\mathcal{N}_\star$ simulations by ensemble averages. Equipartition slows down the gravothermal contraction of the core slightly. Beyond a critical value of $\mu \approx 2$, no equipartition can be achieved between the different masses; the heavy component decouples and collapses. For the first time, the critical boundary between *Spitzer*-stable and *Spitzer*-unstable systems is demonstrated in direct *N*-body models. We also present the measurements of the Coulomb logarithm and discuss the relative importance of the evaporation and ejection of escapers.

Key words: stellar dynamics – galaxies: star clusters.

1 INTRODUCTION

The internal evolution of a star cluster in dynamical equilibrium is governed by its tendency to achieve a thermal velocity distribution (i.e. Maxwellian with energy equipartition) through small changes of velocity during two-body encounters between stars, a phenomenon-dubbed relaxation. The relaxation time is the average time after which a star's moving direction has been deflected by 90° relative to its original orbit (Spitzer 1987). Relaxation produces major changes in the structure of the cluster while keeping it in a dynamical equilibrium.

The collapse of the central core makes up an important phase and probably the most fascinating aspect of the dynamical cluster evolution. There are three mechanisms acting in different ways in order to achieve the collapse: equipartition, evaporation and gravothermal instability. In a real cluster of stars all of these processes are present, but in the idealized models, the ones we will describe; it is possible to isolate the specific processes and gain some understanding of the particular effects.

Spitzer (1969) set about an analysis on segregation of masses in globular clusters systems that would lead later to a broad ensemble of different analyses and techniques. For some clusters, it seemed impossible to find a configuration in which they have dynamical and thermal equilibrium altogether. The heavy component sink into the centre because they cede kinetic energy to the light one on the road to equipartition. In most of the cases, equipartition happens to be impossible, because the subsystem of massive objects becomes self-gravitating before. Thermal energy flows from the inner part to the outer regions. Whereas the outer regions of the cluster do not alter significantly their temperature, the inner regions, the core, loses heat and, so, contracts and becomes hotter. A self-gravitating system has a negative thermic capacity. This phenomenon has been observed in a big number of works using different methods (Hénon 1973, 1975; Spitzer & Shull 1975; Cohn 1980; Marchant & Shapiro 1980; Stodołkiewicz 1982; Takahashi 1993; Giersz & Heggie 1994b; Takahashi 1995; Makino 1996; Quinlan 1996; Spurzem & Aarseth 1996; Drukier et al. 1999; Joshi, Rasio & Portegies Zwart 2000). The late phase of core collapse is the same as for a single-mass model, because the heavy components do not interact with other stars anymore.

There is an ample evidence for mass segregation in observed clusters. McCaughrean & Stauffer (1994) and Hillenbrand & Hartmann (1998) provided a new deep infrared observations of the Trapezium cluster in Orion that clearly show the mass segregation in the system, with the highest mass stars segregated into the centre of the cluster. This is a clear-cut evidence for the mass segregation of stars more massive than $5\,{\rm M}_\odot$ towards the cluster centre and some evidence for general mass segregation persisting down to 1–2 $\rm M_\odot$ in the Orion nebula cluster. Raboud & Mermilliod (1998) studied the radial structure of Praesepe and of the very young open cluster

⋆E-mail: khalisi@ari.uni-heidelberg.de (EK); Pau.Amaro-Seoane@aei.mpg.de (PAS); spurzem@ari.uni-heidelberg.de (RS)

NGC 6231. There, they found evidence for the mass segregation among the cluster members and between binaries and single stars. They put it down to the greater average mass of the multiple systems.

At this point, the question looms up whether for very young clusters mass segregation is due to relaxation, like in our models, or rather reflects the fact that massive stars are formed preferentially towards the centre of the cluster, as some models predict.

To answer such questions, there is a clear necessity for models that give us an accurate description of the evolution of multimass models based on direct-summation numerical schemes.

The simplest case of a bimodal mass spectrum is a starting point to take care of. This is a relatively good approximation if stellar black holes are the heavy components (Lee 1995). Such two-mass simulations are exclusively studied in this work.

Spitzer (1969) gave an analytical criterion to determine whether a two-component system can, in principle, achieve energy equipartition or not. According to his analysis, energy equipartition between the light and heavy component can exist if

$$S := \left(\frac{\mathcal{M}_{\rm h}}{\mathcal{M}_{\rm l}}\right)\left(\frac{m_{\rm h}}{m_{\rm l}}\right)^{3/2} < 0.16, \quad (1)$$

Where $\mathcal{M}_{\rm l}$ and $\mathcal{M}_{\rm h}$ are the total masses in light and heavy stars and $m_{\rm l}$ and $m_{\rm h}$ their individual masses, respectively. Spitzer's work was based on many strong simplifying assumptions.

A number of authors has addressed the problem of thermal and dynamical equilibrium in star clusters from a numerical point of view, with direct *N*-body simulations (Portegies Zwart & McMillan 2000), Monte Carlo simulations (Spitzer & Hart 1971) and with the direct integration of the Fokker–Planck equation (Inagaki & Wiyanto 1984; Kim, Lee & Goodman 1998). As regards the Monte Carlo scheme, recent and very detailed numerical calculations (Watters, Joshi & Rasio 2000) have suggested a different criterion,

$$\Lambda := \left(\frac{\mathcal{M}_{\rm h}}{\mathcal{M}_{\rm l}}\right)\left(\frac{m_{\rm h}}{m_{\rm l}}\right)^{2.4} < 0.32. \quad (2)$$

The limitations inherent in this approach motivate us to embark on more accurate models of this scenario with the help of *N*-body methods, where the Newtonian gravity is essentially treated without approximations.

In his pioneering work, von Hoerner (1960) performed calculations with $\mathcal{N}_\star = 16$ particles on the best computers available at that time. Rapid improvements in computer technology (both hardware and software) facilitated larger as well as more accurate calculations. The amount of 10^4 particles was reached by Spurzem & Aarseth (1996), and parallel machines and special purpose computers do even manage 50 times more nowadays.

In this article, we describe the simulation models based on these methods as well as their initial conditions. We present the results of a wide parameter space, which has been explored by direct *N*-body modelling for the first time. We also extract the important parameters describing the core collapse and equipartition of energies.

2 ORGANIZATION OF THE SIMULATIONS: NOMENCLATURE

For all simulations in this work, we employed a Plummer sphere model in global virial equilibrium. The particles are treated as point masses without softening of the gravitational force, but with regularization of close encounters instead. We only consider two different mass species as the most simple approximation of a realistic mass spectrum. Since this analysis aims to isolate the essential physical process of mass segregation, we ignore stellar evolution, cluster rotation and a tidal field as well as primordial binaries; binary formation occurs only during the late stage of the evolution and do not affect our objectives.

Table 1. Overview of the simulations. A model is described by q and μ and assigned to a capital Roman letter. RND = random set-up; INS = all heavy masses placed inside and OUT = all heavy masses placed outside. As regards series II, $m_{\rm h}$ was inside and outside. The series VI with $\mathcal{N}_\star = 5\times10^3$ can be envisaged as a model for the Orion nebula.

Series	Distribution	q	μ-models	Remarks
I	RND	0.1	A ... H	Various $\mathcal{N}_\star$
II	INS, OUT	0.1	A ... H	$m_{\rm h}$ in/out
III	RND	0.05	K ... R	$\mathcal{N}_\star = 2.5\times10^3$
IV	RND	0.2	T ... Z	$\mathcal{N}_\star = 2.5\times10^3$
V	RND	0.4	T' ... Y'	$\mathcal{N}_\star = 2.5\times10^3$
VI	RND, INS, OUT	0.26	20.0	$\mathcal{N}_\star = 5\times10^3$

In our notation, a model will be determined by its fraction of the heavy-mass component, $q := \mathcal{M}_{\rm h}/\mathcal{M}_{\rm cl}$, and the mass ratio of the individual particles, $\mu : m_{\rm h}/m_{\rm l}$. The model is assigned to a capital Roman letter. Each model consists of a number of runs that differ only in their random number seed which produces different initial set-ups of positions and velocities of the particles for the same distribution function. The runs are physically equivalent. Models making up a logical unit for comparison are gathered to a series (see Table 1).

After the work by Inagaki & Wiyanto (1984), we concentrate on $q = 0.1$ (series I), since this is the value which had the fastest evolution, as they proved, and study the evolution for a wide range of values of μ (from 1 to 50). This choice is guided by observations in youngest star clusters like the Trapezium in the Orion nebula cloud, where a mass range of $\approx$0.1–50 $\mathrm{M}_\odot$ is found (Hillenbrand & Hartmann 1998). This cluster also exhibits clear mass segregation that cannot be explained by the simple theory of 'general' mass segregation driven by two-body relaxation. Given the extreme youth of the stars with highest mass, a primordial segregation has been suggested, in which they were formed at locations close to the dense centre (Bonnell & Davies 1998).

We examine the time-scales for a random set-up of particles (RND) by assigning a mass $m_{\rm l}$ and $m_{\rm h}$ to each body. For μ is a relative quantity, we fix $m_{\rm l}$ to unity, and vary $m_{\rm h}$ in steps that are given in the top row of Table 2. The two-mass populations have $\mathcal{N}_{\rm l}$ and $\mathcal{N}_{\rm h}$ members (we will elaborate on this ahead), whose spatial coordinates, positions and velocities are picked up randomly according to a Plummer sphere (Aarseth, Henon & Wielen 1974).

In series II, we place the heavy particles completely either in the centre (INS) or in the outskirts (OUT) and compare the evolutionary patterns with the random set-up of series I. In series III–V we alter the fraction of heavy masses, q, to test for this parameter. The full parameter space is graphically illustrated in Fig. 1. Additionally, we performed simulations of a special configuration, which is related to a mass ratio in the Orion nebula cloud (series VI).

In order to reduce the statistical noise, we performed a large number of runs and averaged the data set into an ensemble model. The statistical quality of such an ensemble averaging is comparable with one single calculation containing the full particle set of all runs (Giersz & Heggie 1994a). This means that, since the fiducial model is a cluster with $\mathcal{N}_\star = 2.5\times10^3$ particles, we carried out 20 runs and the whole set containing $\mathcal{N}_\star = 5\times10^4$ has as little

Table 2. Absolute numbers of heavy stars for the models of series I. Next to each model, we give the value for μ in brackets.

$\mathcal{N}_\star$	A (1.25)	B (1.5)	C (2.0)	D (3.0)	E (5.0)	F (10.0)	G (25.0)	H (50.0)
10^3	82	69	53	36	22	11	4	–
2.5×10^3	204	172	132	89	54	27	11	6
5×10^3	408	345	263	179	109	55	22	11
10^4	816	690	526	357	217	110	44	22
2×10^4	1633	1379	1053	714	435	220	88	44

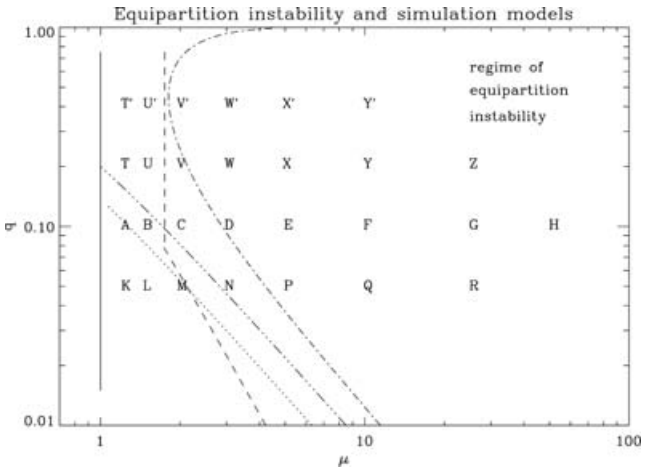

Figure 1. Parameter space of the models examined in this work. The position of the Roman letters indicate a model determined by its q and μ. The dotted line is the boundary of the equipartition stable region after Spitzer (1969), the dash–dotted line is the stability criterion after Lightman & Fall (1978), the dot–dot–dot–dashed line is the prediction by Inagaki & Wiyanto (1984) and the dashed line is the empirically proposed condition by Watters et al. (2000).

noise as a high-$\mathcal{N}_\star$ model. In series I, we also performed 50 runs for $\mathcal{N}_\star = 10^3$, and 10 runs for $\mathcal{N}_\star = 5 \times 10^3$. Additional models containing 10^4 particles (four runs) and 2×10^4 particles (one run) were also performed.

2.1 Parameters of two-mass models

In order to describe the physics of our models, we have to define a set of three parameters:

$$\mathcal{N}_\star = \mathcal{N}_\mathrm{l} + \mathcal{N}_\mathrm{h}, \quad \mu = \frac{m_\mathrm{h}}{m_\mathrm{l}}, \quad q = \frac{\mathcal{M}_\mathrm{h}}{\mathcal{M}_\mathrm{cl}}. \tag{3}$$

Since the number of the force calculations per crossing time-scales with $\mathcal{N}_\star^2$, computational efforts restrict the choice of $\mathcal{N}_\star$. We can express $\mathcal{N}_\mathrm{l}$ as follows,

$$\begin{aligned} q &= \frac{\mathcal{M}_\mathrm{h}}{\mathcal{M}_\mathrm{l} + \mathcal{M}_\mathrm{h}} = \frac{m_\mathrm{h}\mathcal{N}_\mathrm{h}}{m_\mathrm{l}\mathcal{N}_\mathrm{l} + m_\mathrm{h}\mathcal{N}_\mathrm{h}} \\ &= \frac{m_\mathrm{l}\mu\mathcal{N}_\mathrm{h}}{m_\mathrm{l}\mathcal{N}_\mathrm{l} + m_\mathrm{l}\mu\mathcal{N}_\mathrm{h}} \\ &= \frac{\mu(\mathcal{N}_\star - \mathcal{N}_\mathrm{l})}{\mathcal{N}_\mathrm{l} + \mu(\mathcal{N}_\star - \mathcal{N}_\mathrm{l})}. \end{aligned} \tag{4}$$

The absolute number of light particles is then

$$\mathcal{N}_\mathrm{l} = \frac{(1-q)\mu\mathcal{N}_\star}{q - \mu q + \mu}. \tag{5}$$

Some authors (e.g. Inagaki & Wiyanto 1984) define a slightly different parameter $\hat{q} := \mathcal{M}_\mathrm{h}/\mathcal{M}_\mathrm{l}$. With this definiton, equation (5) turns out to be $\mathcal{N}_\mathrm{l} = \mu\mathcal{N}_\star/(\hat{q} + \mu)$. In the following, we employ the notation of Spurzem & Takahashi (1995), as defined in (3). The absolute numbers of the heavy particles, $\mathcal{N}_\mathrm{h} = \mathcal{N}_\star - \mathcal{N}_\mathrm{l}$, are shown in Table 2 for the models of series I ($q = 0.1$). μ is given in brackets on the top of each column.

A different way of fixing the mass ratio μ is by means of the average mass of the stars:

$$\tilde{\mu}_i = \frac{m_i}{\langle m \rangle}, \tag{6}$$

where $\langle m \rangle = \mathcal{M}_\mathrm{cl}/\mathcal{N}_\star$ and m_i is the ith component in a multimass cluster. With $q_i = \mathcal{M}_i/\mathcal{M}_\mathrm{cl}$, we have for the general case of k different mass components

$$\mathcal{N}_i = \frac{q_i\mathcal{N}_\star}{\tilde{\mu}_i} = \frac{\langle m \rangle q_i \mathcal{N}_\star}{m_i} = \frac{\mathcal{M}_i}{m_i} \tag{7}$$

particles in the ith mass bin.

The advantage of this expression lies in the simpler handling, if more than two masses are present. In the equation (5), $(k-1)!$ parameters of m_i/m_j would be necessary for k mass components, while employing $\langle m \rangle$ reduces the amount of the *a priori* definitions of the values of m_i to $k-1$.

3 RESULTS FOR $\mathcal{M}_\mathrm{h}/\mathcal{M}_\mathrm{cl} = 0.1$

In this section, we deal with the situation in which the fraction of heavy stars makes up 10 per cent of the whole cluster mass. We investigate the physical processes occurring from a random initial distribution and compare them with previous literature on this subject. The essential facts about the evolution are qualitatively visible in Fig. 2. The core radius shrinks with time, and the cluster collapses under its self-gravity. The shorter the time-scale for the collapse the larger the mass ratio μ between heavy and light stars is. The formation of binaries in the core stops the collapse and allows its re-expansion. We focus our attention on the variations of the evolutionary processes for different values of μ.

3.1 Data of ensemble averages

We vary μ from 1.25 to 50.0 and obtain the core-collapse time, t_cc, for each run by considering two values: first, the moment of the minimum core radius, $t(\mathrm{r_c}|_\mathrm{min})$ and, second, the deepest central potential, $t(\Phi|_\mathrm{min})$. The output data were written for each N-body time unit. Because of large fluctuations between two subsequent data points, we applied a 'sliding average' over r_c and Φ, based on the following algorithm

$$\mathcal{R}_i = \frac{1}{w}\sum_{j=0}^{w-1} \mathcal{A}_{i+j-w/2}, \tag{8}$$

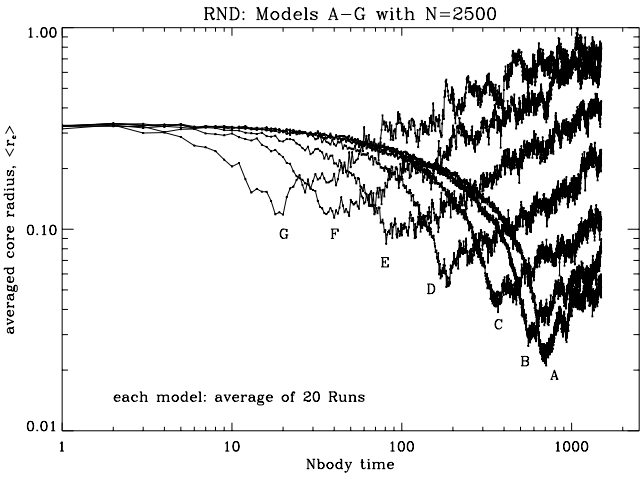

Figure 2. Comparison of the shrinking core radius in the models A–G of series I given in NBODY units (see Appendix B).

where $\mathcal{R}_i$ is the resulting value of the original variable $\mathcal{A}_i$ averaged among w neighbouring data points. The choice of $w = 5$ turned out to be the best-fitting one.

The average of the times found from the minima of r_c and Φ is defined to be the core-collapse time of the run:

$$t_{cc} = \frac{t_{r_c} + t_\Phi}{2}. \tag{9}$$

Fig. 3 illustrates the distribution of the data points of r_c and Φ_{min} at their corresponding core-collapse times for four selected models. The logarithmical time-axis was chosen to show the relative scatter between the point clouds. When looking at a particular run, the core-collapse times are likely to show a significant discrepancy between the determination from the potential or the core, i.e. t_Φ does not necessarily correspond to t_{r_c}, but the averages of both, $\langle t_{r_c}\rangle$ and $\langle t_\Phi\rangle$, yield a good concordance for the whole model. Thus, $\langle t_{cc}\rangle$ is a good value to characterize the core-collapse time of the model,

$$\langle t_{cc}\rangle = \frac{\sum\left[(t_{r_c} + t_\Phi)/2\right]}{\mathcal{N}_{runs}} = \frac{\langle t_{r_c}\rangle + \langle t_\Phi\rangle}{2}. \tag{10}$$

In this last equation, $\mathcal{N}_{runs}$ is the number of runs and we obtain an equality between the left- and right-hand side by linearity.

As we can see in Fig. 3, the relative variance of the core-collapse times increases for smaller values of $\langle t_{cc}\rangle$. The mean values for the eight models of our series I are summarized in Appendix A. The errors given there are the standard deviation from the runs' mean t_{cc}, divided by the square root of the number of the runs $\sqrt{\mathcal{N}_{runs}}$. The error of $\langle t_{cc}\rangle$ is roughly 2–5 per cent for most of the models, consistent with the relative errors determined by Spurzem & Aarseth (1996) and the half-mass evaporation times by Baumgardt (2001).

4 EVOLUTION OF THE CORE RADIUS

The evolution of the core radii for the models A–G is plotted in Fig. 2. Each curve is an ensemble average of 20 runs. For models with μ approaching unity, the core radius shrinks as in an equal-mass system (at late collapse times, to the right). A linear time-scale (not shown here) suggests that the collapse phase sets in when the core radius has contracted to about 25 per cent of its initial radius. This is in agreement with the results of Giersz & Heggie (1994a). For high values of μ, this happens from the start of the simulations. The rapid contraction of r_c is due to the very massive stars falling quickly to the centre. The contraction stops at higher r_c-values than for the low-μ models, and a quick expansion of the core follows.

The behaviour at the moment of core bounce is illustrated in Fig. 4, where the minima of the potential and the core radius are plotted versus μ. For a fixed $\mathcal{N}_\star$ and values of μ between 3 and 10, the core collapse is carried out by approximately the same number of particles, but they do not draw together as close as for the equal-mass case or very small values of μ. Therefore, the density and the central potential are less deep than those for $\mu \lesssim 2$, and the minimum of the core radius is not so profound. At high values of μ, the effect is reversed. Even some few heavy components are massive enough to deepen the potential. The collapse itself is less distinct, as seen from the shallower r_c in the right-hand panel. In this range of values for μ, the depth of the potential results from the combination of these two effects. Heavy masses build up a strong gravitational field, but their kinetic motion does not allow a long-lasting vicinity. Equipartition becomes then impossible. The differences of the depths for various $\mathcal{N}_\star$ are discussed in Section 8.

For a system in which the central object has a small mass and the energy production is confined to a small central volume we have that the core radius r_c should follow an expansion proportional to

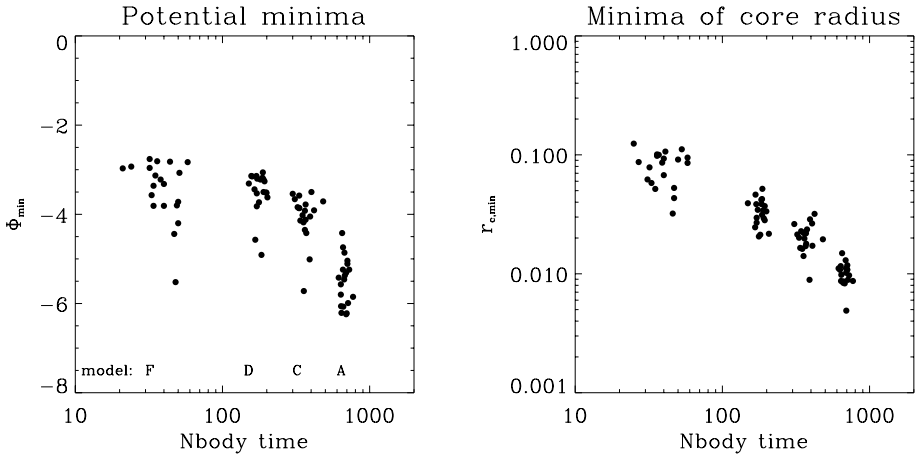

Figure 3. Models A, C, D, and F of series I with $N_\star = 2500$. Each point represents the minimum value of the central potential Φ_c (left-hand panel) and core radius r_c (right-hand panel) at the time when these parameters attain their minimum. The average values for all models are listed in the appendix.

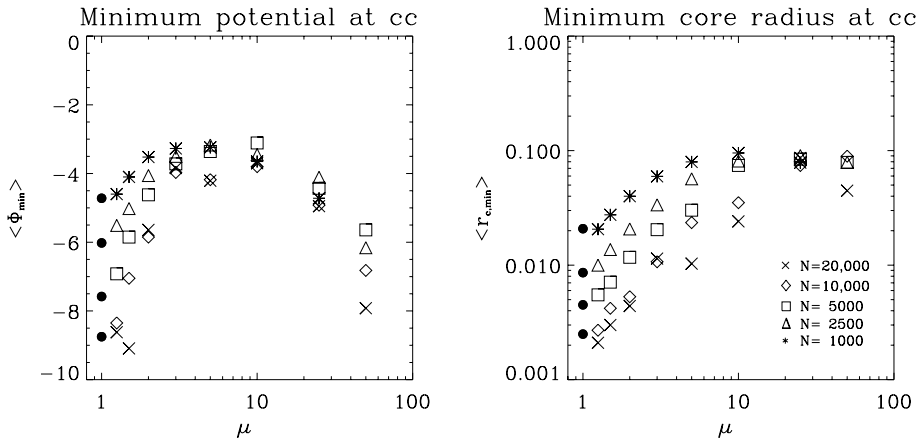

Figure 4. Minima of potential (left-hand panel) and core radius (right-hand panel) at the moment of core bounce. The collapse is carried out by a less number of core particles when μ rises. The filled circles correspond to the single-mass case. See the text for explanations in more detail.

Table 3. Measured exponent for core-radius expansion in the post-collapse phase. See the text for further explanation.

Slope	A	B	C	D	E	F	G
Up	0.631	0.666	0.680	0.525	0.522	0.490	0.420
Low	0.940	0.864	0.662	0.615	0.524	0.517	0.445
Mean	0.7855	0.765	0.671	0.570	0.523	0.5035	0.4325

the power law of t and t_{cc} (Hénon 1965; Shapiro 1977; McMillan, Lightman & Cohn 1981; Goodman 1984),

$$r_c \propto (t - t_{cc})^{2/3}. \tag{11}$$

We measured the slopes of the expanding values of r_c in Fig. 2 by fitting two straight lines embracing the fluctuating data of each model to construct an upper and a lower margin. These lines give two independent measurements for the slope and are presented in Table 3, and they show a decreasing trend for higher μ.

The lower lines seem to be steeper than the upper ones for the most of the models. On the other hand, the simulations reach different stages of the post-collapse evolution, and the expanding branches exhibit different lengths. Especially, the low-μ models (A and B) are not far advanced for precise measurements, while the high-μ models (F and G) appear distorted about the time of collapse such that the onset of the self-similar expansion is difficult to find (see also Giersz & Heggie 1994b). From the theoretical point of view, there is no argument for a different behaviour of the core expansion when unequal masses are present.

5 CORE-COLLAPSE TIMES

As we explained in Section 1, the two-body relaxation causes star clusters to redistribute the thermal energy among stars. Since this kind of heat transfer acts on the relaxation time-scale, a core collapse is similarly ensued in gravitationally unstable systems.

The core-collapse time is best studied numerically. For equal-mass models, it ranges about $t_{cc} \approx 330\, t_{rc}(0)$ during the self-similar phase. or about 12–19 half-mass relaxation times (Quinlan 1996). In this article, Quinlan gives a time-scale of $15.7 t_{rh}$ for an isolated cluster, if an isotropic velocity distribution is assumed. Takahashi (1995) also modelled Plummer spheres but for an anisotropic case, and determined the collapse time to about $17.6\, t_{rh}$. Other authors find similar factors, and we will adopt

$$t_{cc} \approx 17.5 t_{rh}. \tag{12}$$

Though the values are used in most studies of the core collapse, they are a poor guide for clusters with a mass spectrum, e.g. globular clusters have central relaxation times that are typically ten, sometimes a hundred times shorter than their half-mass relaxation times (Quinlan 1996; Gűrkan, Freitag & Rasio 2004).

So far, the core-collapse time is only found empirically from a large number of numerical simulations, for there exists no analytical theory which would predict it *a priori* from cluster properties, e.g. the star number, the initial mass function, or the concentration parameters.

It has been suggested that the nucleus consisting of two mass components collapses in a time shorter than the equal-mass cluster by a factor of $1/\mu$ (Fregeau et al. 2002). In broad terms, this is so because the equipartition time is shortened according to the time-scale for equipartition (Spitzer 1969). The upper panel of Fig. 5 shows detailed calculations in a wide μ-range of this. The mean times, $\langle t_{cc} \rangle$, have been plotted versus μ for the complete sample of our models in series I.

In the upper panel, the core-collapse times converge smoothly to the collapse time for an equal-mass cluster, $t_{cc,1}$, as μ approaches unity. Between $\mu \approx 2$ and 10, a somewhat linear decline is visible, but far beyond the stability boundary, run towards a constant value, since binaries are likely to have more importance when the value of μ is larger. In the same figure, in the lower panel, we display the factor of 'collapse acceleration' for various values of μ. This gives us a measure to which percentage a cluster with two masses evolves faster than the single-mass case. The dashed line is the μ^{-1}-decline, i.e. a cluster with two mass species having a ratio μ would collapse μ-times earlier than its single-mass equivalent according to

$$t_{cc,\mu} \propto \frac{1}{\mu} t_{cc,1}. \tag{13}$$

At $\mu = 2$, the decoupling of the equipartition-based instability and the gravothermal instability seems to take place. For $\mu \longrightarrow 1$, the evolution occurrs more slowly than the $1/\mu$-decrease, because the tendency to equipartition drives the initial evolution and slows down a 'purely' gravothermal collapse. This seems to suggest that as the mass difference between m_h and m_l becomes less important, the system collapses like a single-mass cluster. Beyond the critical value $\mu = 2$, an early decoupling of the two-mass populations occurs. The heavy components try to reduce their large velocity dispersion, but

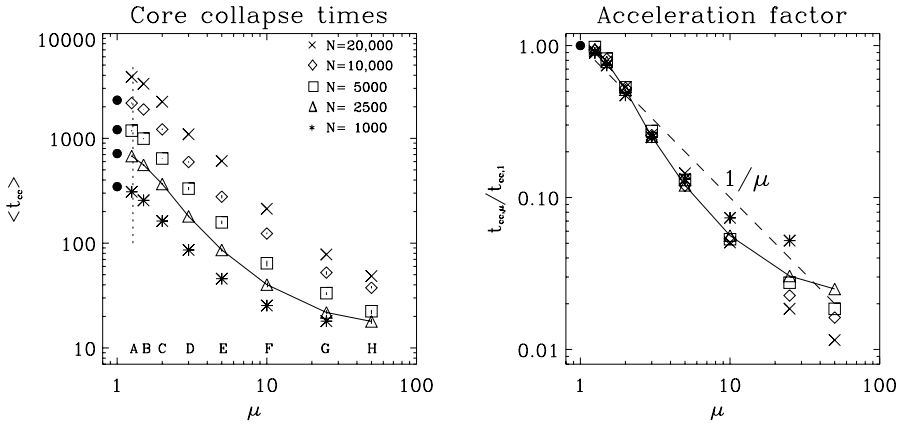

Figure 5. Left-hand panel: core-collapse times of the models in series I. The times shorten non-linearly with increasing μ. The dotted line at $\mu = 1.275$ is the equipartition criterion given by Spitzer (1969, equation 3–54) for a value of $\chi_{\max} = 0.16$ and $q = 0.1$. The core-collapse times of the corresponding equal-mass clusters are indicated by filled dots. The error bars are smaller than the symbols. In the right-hand panel all collapse times are normalized to $t_{\rm cc,1}$ (the core-collapse time for the single-mass case). The simulations for $N_\star = 2.5 \times 10^3$ are connected with a solid line for clarity. The circles at the left-hand side are the collapse times for an equal-mass cluster according to equation (12), and the dotted line is the stability boundary by Spitzer with $\chi_{\max} = 0.16$ (Spitzer 1987, equation 3–55).

they rapidly accumulate in the centre and interact preferably with themselves. As a consequence, equipartition is harder and harder to achieve and the evolution proceeds only due to the redistribution of heat within the two, almost separated components (Bettwieser & Inagaki 1985). The light stars evaporate out of the core and take away the thermal energy to the outskirts, while the heavy components increase their binding energy. The latter ones collapse like a single-mass subcluster. The release of energy transported away and the heat transfer works effectively and leads to an accelerated collapse.

If $\mu \gg 1$, the situation turns into a case of dynamical friction. A significant fraction of particles are drowned into a homogeneous sea of light stars and, like in an ordinary frictional drag, their motion suffers a deceleration. It is instructive to see that only for large $\mathcal{N}_\star$, the absolute number of heavy stars seems sufficient to maintain the linear slope of accelerated cluster evolution. The slope follows the dashed line a bit longer before bending towards that constant value.

6 MASS SEGREGATION

The process of mass segregation for the six models A–F is illustrated in Fig. 6, where the mean mass of the stars that are inside a specified Lagrangian shell, is shown (i.e. a Lagrangian shell is the volume between two Lagrangian radii, which contain a fixed mass fraction of the bound stars in the system; see Giersz & Heggie 1994a). With the light and heavy masses randomly distributed, each shell exhibits the same average mass at the beginning. In the course of the evolution, the inner shells assemble the heavy bodies, and raise the mean mass. The half-mass radius and the outer shells lose their heavy stars rather quickly and remain below the value for the average mass, because the light ones outnumber the heavy components significantly. The cluster is stratified by the mass.

The segregation of masses propagates simultaneously with the contraction of the core. Giersz & Heggie (1996) have already noted the self-similarity of this process. In the models A and B, we can clearly see how the inner layers decouple stepwise one after the other until the final stage is reached. After the collapse, the profile does not change much; the effect has only influence on the early evolutionary phase, not in the post-collapse. The moderate decline in the models E and F can be explained by the escaping of heavy particles. Because of their relatively small absolute number (see Table 2), they get ejected from the core and leave the cluster so that the surplus of small bodies depletes the mean value in the shells. A fraction of high-mass stars in the centre interact strongly in a few-body process and kick out each other, and the core is gradually 'evacuated' from the heavy stars. In our data, we find an enhanced fraction of high-mass escapers occurring immediately after the collapse confirming this scenario; many of them exhibit enormous kinetic energies and some even escape as bound binaries (see Section 7). However, some heavy latecomers enter the inner regions, but a balance is found between the incoming and outgoing mass flux. In general, the dynamical processes in the core do not influence the properties of the cluster as a whole.

The mean mass in the 1 per cent Lagrangian shell never attains its full 'capacity', i.e. the value of $m_{\rm h}$ that could principally be gained if this shell was completely populated by heavy stars; which is only possible if the heavy stars are 51 per cent. It means that there is always a number of low-mass stars entering and leaving the innermost region that keep $\langle m \rangle_{1\,\rm percent}$ at a constant fraction of the maximally attainable level. This level is at about $0.8\,m_{\rm h}$ if μ is small, and drops to $0.5\,m_{\rm h}$ for the highest values of μ.

Another illustration of the segregation process is given in Fig. 7. It shows the shrinking distance moduli of 18 heavy-mass stars of one typical run of a model with a high mass ratio (model G, $\mu = 25$, Run no. 4, $\mathcal{N}_\star = 5 \times 10^3$); this model consists of 22 heavy-mass stars initially, but four stars escaped at some time before the moment for which we show the plot and they were excluded from it. 17 dashed lines were overlapped demonstrating how the orbits of most particles draw rapidly closer. The core collapse occurs at $t_{\rm cc} = 33.5$. A solid line lifts off one particle of example that was knocked out of the chaotic region due to a close encounter, but its kinetic energy was not sufficient enough to leave the system and it segregated inwards again. One other particle, whose pericentre was at $0.9\,N$-body radii, remained in the halo and did not take part in the collapse, but it sank to intermediate distances at about $t_{\rm cc} \approx 70$.

7 ESCAPERS

The estimation of escape rates is often based on idealized models, whose simplifying treatments sometimes lead to different results. The complexity of this topic is reviewed by Meylan & Heggie

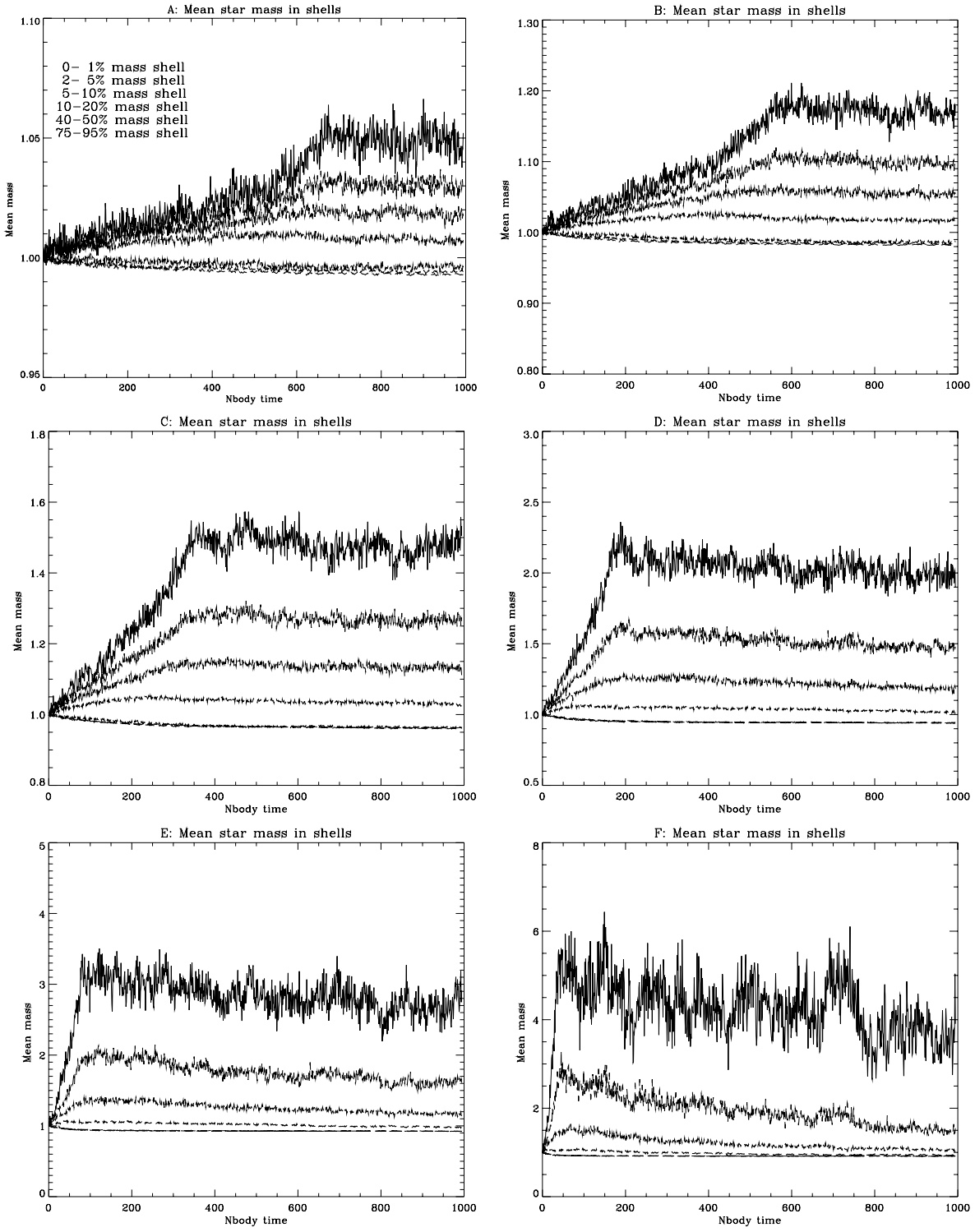

Figure 6. Average mass in Lagrangian shells for models A–F shows the stratification of masses in the cluster. The segregation of heavy masses proceeds in agreement with the global evolution of the cluster. The mean mass is indicated.

(1997). For the results that we show in this work, we should mention the following.

(i) Theories based on diffusive or small-angle relaxation phenomena yield a different escape rate than theories involving individual two-body encounters. The former is often denoted as 'evaporation', the latter is related to 'ejections', which dominate for isolated clusters, like here.

(ii) The rate of escape is not a constant, while the evolution of the system proceeds, even in the pre-collapse phase.

(iii) An increasing concentration in the core as well as the growth of anisotropy tends to enhance the escape rate.

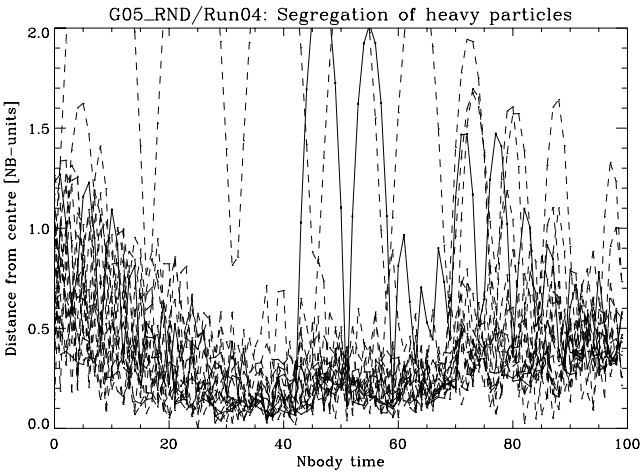

Figure 7. Distance moduli of 18 heavy mass particles in model G with $N_\star = 5 \times 10^3$. Each of the particles has a mass 25 times larger than a light particle (orbits not shown). The core collapse of this run occurred at $t_{\rm cc} = 33.5$.

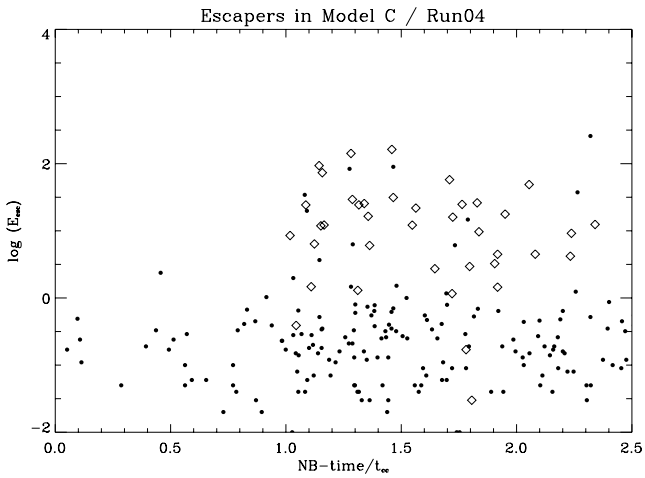

Figure 8. Model C ($\mu = 2.0$), Run no. 04, with $N_\star = 5 \times 10^3$. Energy of an escaping particle is given in units of kT and plotted against its escape time scaled to the core collapse. Diamonds denote heavy masses.

(iv) Furthermore, the escape rate is strongly mass dependent; different mass spectra and segregation alter it.

(v) A tidal field lowers the energy threshold for escape.

(vi) A sufficient abundance of binaries (both, primordial and formed) has a substantial effect on high-velocity escapers which take away energy from the system.

In view of these complications, we have to take care in the interpretation of the data. We show in this section *N*-body simulations investigating the rates for various particle numbers and the variation on μ, in particular.

An escape is defined by a particle having both positive energy and its distance from the density centre exceeding a limiting radius. We have chosen the distance to be 20 times the half-mass radius, $r_{\rm h}$.

The particles were removed from the calculation when both conditions were fulfilled; we will call them 'removed escapers'. We focus here on escapers occurring before the time of core collapse, $t_{\rm cc}$. One run contains a number of particles which have gained positive energy but not reached the distance for a removal yet. Such kind of particles dominate when $t_{\rm cc}$ is very short. In particular, the high-μ models collapse within a few tens of *N*-body time units, and a large number of particles, that are going to escape, would be missed. This situation resembles the 'energy cut-off' (Baumgardt 2001), and we will call these particles 'potential escapers'. Whether some of them will be scattered back to become bound members again or really escape, is a complex process that is out of the scope of our subject. Baumgardt (2001) estimated that a fraction of 2 per cent of the potential escapers might return to the system. As a first approach to the general properties of escapers, we will assign to the number $\mathcal{N}_{\rm esc}$ all removed escapers plus potential escapers at the epoch of $t_{\rm cc}$. Because of the scatter of the core-collapse times (Section 3.1), each run was checked separately for its escapers that occurred before that run's individual core-collapse time – not the ensemble's $\langle t_{\rm cc}\rangle$. $\langle\mathcal{N}_{\rm esc}\rangle$ is the average among the individual values of $\mathcal{N}_{\rm esc}$.

Fig. 8 gives a typical example for the energy distribution of all removed escapers in the one run of model C with $\mathcal{N}_\star = 5 \times 10^3$; the potential escapers are disregarded here. The energy is plotted against the time of removal; it is measured in units of $kT = \bar{m}\sigma_{0,av}^2$, where $\bar{m}$ is the average mass and $\sigma_{0,av}$ the average 1D velocity dispersion in the core, measured for the initial model. Light bodies are represented by filled dots, heavy ones of $m_{\rm h} = 2.0$ by diamonds. The collapse occurred at $t_{\rm cc} = 643.5$ for this run. In the beginning, the light particles diffuse slowly from the system with small energies (the evaporational effect). After the core collapse, the mass dependence is more complicated, for a second class of escapers joins: high-energy particles, whose energies are higher by two orders of magnitude. A fair fraction of the escapers are heavy stars. As in the statistics for equal masses by Giersz & Heggie (1994a), it is natural to associate them with ejected stars that go back to three-body interactions in the very centre. Mass segregation has widely finished at the time of core collapse, and interactions in the core start depleting the high-mass population. Other runs of the same model exhibit a similar picture of the physical scenario.

The analysis of the models in regard to μ reveals interesting views on the escape mechanism. A summary is shown in Fig. 9, and the legend for the symbols is given in panel (e). Panel (a) gives the fraction of escaped stars, $\langle\mathcal{N}_{\rm esc}\rangle/\mathcal{N}_\star$. In a single-mass cluster ($\mu = 1$), about 2.5 per cent of the stars leave the system before it collapses. When introducing a second mass, this fraction drops to 0.2–0.5 per cent until $\mu \approx 3$. The reason is that the rate of escape (panel e) is nearly constant for small μ, but the shorter collapse times cause a smaller progress of the escape mechanism, and thus a smaller $\mathcal{N}_{\rm esc}$. When massive bodies $m_{\rm h} \gg m_{\rm l}$ are present, a larger fraction of stars receives positive energy and turns into potential escapers.

Panel (b) gives the ratio of the removed escapers to the potential escapers as described above, $\langle N_{\rm rem}\rangle/\langle\mathcal{N}_{\rm pot}\rangle$. For μ close to the equal-mass case, the core-collapse time is large. Thus, the accumulated number of removed particles is larger by $\approx$10 times than the number of potential escapers at the moment of $t_{\rm cc}$. For high values of μ, removed particles are scarce, while potential escapers did not have time to cross the cluster and turn into removed ones. Therefore, the potential escapers make the overwhelming majority. The slope of the decrease is -1, and it is similar to the shortening of $t_{\rm cc}$ when μ increases. The vertical dependence on $\mathcal{N}_\star$ mirrors the increasing amount of removed escapers due to the longer $t_{\rm cc}$ times for larger $\mathcal{N}_\star$.

Panels (c) and (d) deal with the individual masses of the escapers. When one heavy star escapes, it raises the average escaper mass. In the models $\mu \gtrsim 10$, the absolute number of high-mass escapers is zero for most of the runs. This is the converse situation of

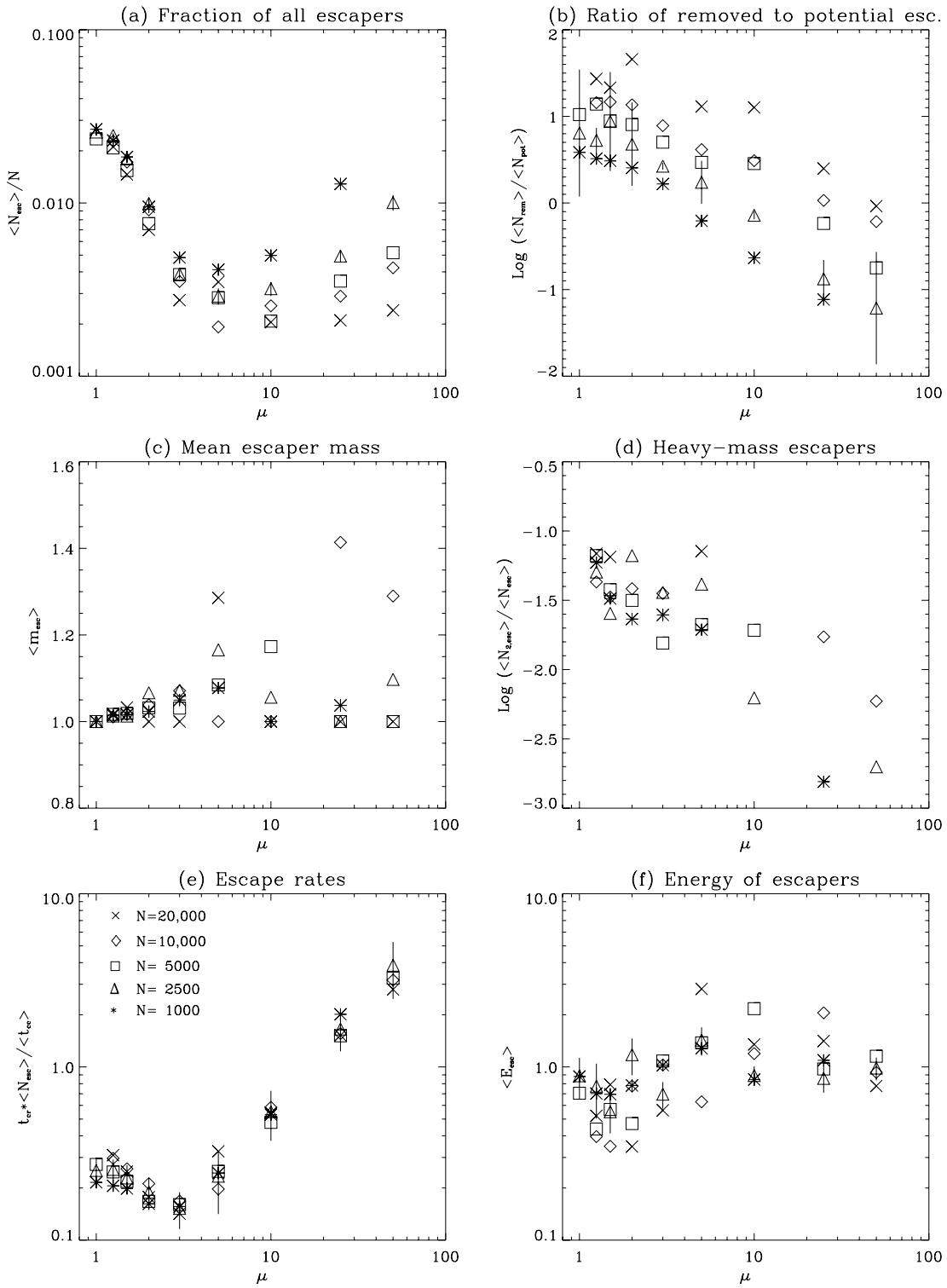

Figure 9. Summary of escaper data for the different models. (a) Fractions of removed escapers before the core collapse plus potential escapers at $t_{\rm cc}$. (b) Ratio of removed escapers to potential escapers. (c) Mean mass of escapers. (d) Relative number of $m_{\rm h}$-escapers among all escaping particles. (e) Escape rates. (f) Mean energy of escapers in kT. The error bars are usually omitted, though they are given for the $N_\star = 2.5 \times 10^3$ set (triangles) except in the panels (c) and (d); the error bars are almost invisible in (c), and larger than the panel size in (d), because the number of high-mass escapers varies a lot among one model.

panel (a): for massive stars, the escape is difficult. Just one or two heavy components appear and take away a significant fraction of mass from the cluster. They are rather evaporated objects than ejected in a close encounter, because their energies are relatively small. Usually, the heavy escapers occur in the late post-collapse phase and do not receive our attention here. From panel (d) and $\mu \leqslant 5$, we find that ≈3 per cent of all escapers are heavy components which leave the system before $t_{\rm cc}$.

Panel (e) presents the rates of escape within a crossing time for different μ. The computation was adopted from Wielen (1975) as

$$\left\langle \frac{\mathrm{d}\mathcal{N}_\star}{\mathrm{d}t} \right\rangle = t_{\rm cr} \frac{\langle \mathcal{N}_{\rm esc} \rangle}{\langle t_{\rm cc} \rangle}, \tag{14}$$

where the brackets denote averages among the runs within a model and $t_{\rm cr}$ is the average number of escapers per crossing time. For equal-mass clusters our rate is ≈0.2—0.3 in accordance with other N-body results listed by Giersz & Heggie (1994a). The slight decline until $\mu \approx 3$ and the stronger increase afterwards is in excellent agreement with the theoretical expectation by Hénon (1969) (Fig. 1). Though his models differ from ours in q, the branch of the curve related to our models exhibits the same shape. We interpret the curve such that two different mechanisms produce escapers in the pre-collapse phase under consideration. Relaxation dominates if the individual masses do not differ much, thus evaporation causes a steady mass loss from the system. When μ is increased slightly, the effect of evaporation cannot advance so far. The escape rate is reduced then. For higher values of μ another mechanism takes over. Massive stars exhibit a strong gravitational focusing. The gravity of one single heavy particle attracts more light stars and its energy is distributed among them. So, a multitude of light stars easily gains positive energy and heads for escape. The frequent two-body encounters of one heavy particle leads rather to ejections involving high energies than an accumulation of small escape energies.

Panel (f) of Fig. 9 shows the mean energy carried away by the stars. The near constancy suggests an independence on μ, but a subdivision into removed and potential escapers (not shown here) reveals differences between the two groups. For removed escapers, the mean energy increases as much as a factor of 10 over the whole μ-range. This confirms the ejection scenario explained for panel (e). On the other hand, the potential escapers show a constant but somewhat lower energies on an average. Since they make up the larger fraction, the mean is depleted in the high-μ regime.

Finally, we can conclude that models resembling the equal-mass model tend to lose their mass by a slow evaporation process, while energetic ejections outweight in high-μ models. At $\mu \approx 3$, both processes are exchanging their dominant role. After mass segregation has come to a stop near core bounce, three-body encounters in the core start depleting the population of $m_{\rm h}$-stars.

8 LARGER PARTICLE NUMBERS

Some dependencies on different particle numbers have already been dealt in the foregoing sections. Here, we present a direct comparison of the cluster evolution for the A models first. This model is close to the uniform mass case and has the longest evolution time. Fig. 10 shows the raw data of the minimum potential for five runs, i.e. we applied no smoothing or averaging.

The most obvious feature, is the increasing core-collapse time in pretty accordance to the increasing relaxation time proportional to $\mathcal{N}_\star/\ln(\gamma\mathcal{N}_\star)$ (see Section 8.1). Note that the fluctuations of the data in the pre-collapse phase are smaller for higher $\mathcal{N}_\star$, because the global potential is smoother. In the post-collapse, the fluctuations are nearly the same, for the number of core particles, $N_{\rm c}$, is of the same order for each of the five runs.

The assumed constancy of $\mathcal{N}_{\rm c}$ (where the subscript 'c' stands for core) leads to a second topic concerning the different amplitudes of the potential minima. This has already been mentioned in connection with Fig. 4, though the upper panel of Fig. 11 points to the variations on $\mathcal{N}_\star$ in a more clear way. For models resembling

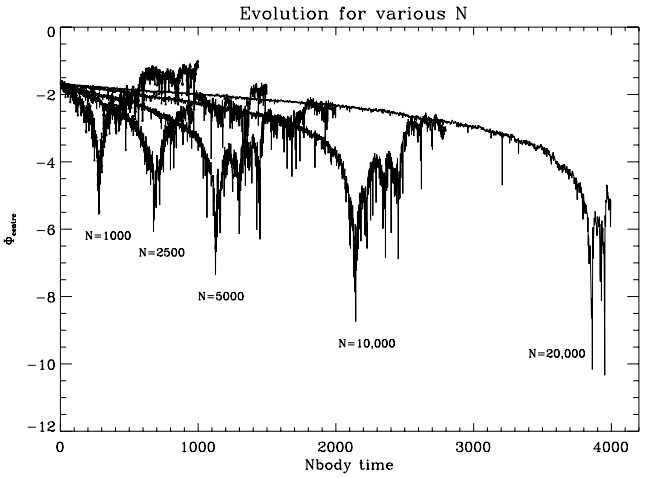

Figure 10. Evolution of the central potential of selected runs of model A for $N_\star = 10^3,\ 2.5 \times 10^3,\ 5 \times 10^3,\ 10^4$ and 2×10^4 particles.

the equal-mass case, the maximum depth is a function of $\mathcal{N}_\star$. The reason is that the collapse is only halted when the rate of energy production in the core becomes the same as the energy rate going out via the heat flux of the gravothermal instability (Goodman 1987). The outflowing energy is produced by the formation of binaries in three-body encounters, and this become important when the density is sufficiently high. As the core radius of a large-$\mathcal{N}_\star$ cluster contains a larger number of stars initially, it has to get rid of almost all of them. The final $\mathcal{N}_{\rm c}$ at core bounce is nearly a constant and the evolution of the core radius advances deeper in order to provide the density necessary for binary formation. Giersz & Heggie (1994b) described this scenario in terms of the fraction of core radius to half-mass radius, $r_{\rm c}/r_{\rm h}$: the larger $\mathcal{N}_\star$, the smaller is that fraction. This is visible for models with μ close to unity in Fig. 11. Though, the lower panel suggests a slight increase of core particles for large-N models, the absolute values of $\mathcal{N}_{\rm c}$ stay in the order between 10 and 40.

The situation looks somewhat different for models with high μ, in particular for $\mu = 25$ and 50. The central potential shows its deepest value when some of the heavy masses have gathered in the core, while the light stars have not changed their density distribution. The presence of the massive stars causes the deeper potential, and it appears not as profound as for nearly equal masses (see Fig. 4 for comparison). Therefore, the amplitude of the collapse, $\langle \Phi_{\rm min} \rangle$, depends on $\mathcal{N}_{\rm c}$ only weakly.

8.1 The Coulomb logarithm

Now, we will focus on the coefficient γ in the Coulomb logarithm, which is of relevant importance for the evolution of the star cluster, because it is intimately connected with the time-scale associated with the evolution of the cluster, the relaxation time (equation 2–62 of Spitzer 1987). The value of this quantity, $\ln(\gamma\mathcal{N}_\star)$, has been estimated to be $\gamma = 0.11$ (Giersz & Heggie 1994a) for a single-mass cluster, but the variations on μ are not known precisely. One possible way to determine this quantity is by comparing the evolution of the same model but for different values of $\mathcal{N}_\star$.

The upper panel of Fig. 12 shows the ensemble-averaged Lagrangian radii of our model A for two different $\mathcal{N}_\star$. For the time t, the value of a Lagrangian radius in the 2500-body model was

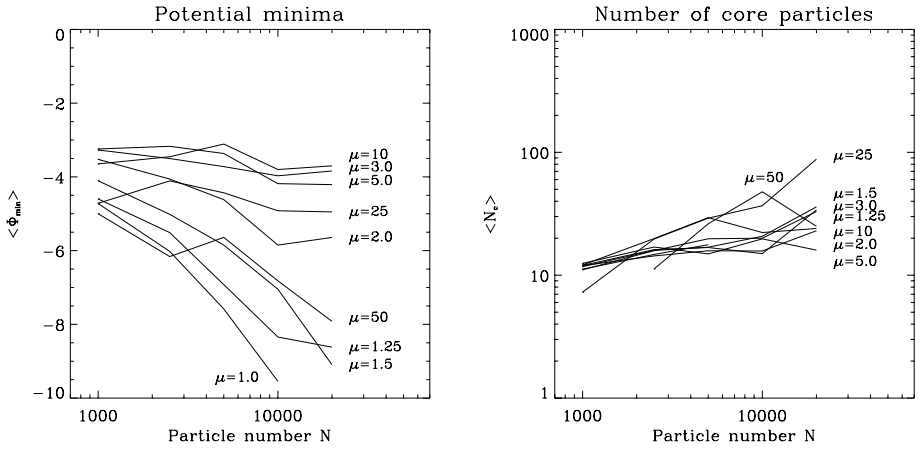

Figure 11. Upper panel: the mean potential minima at the moment of core bounce as as function of the total particle number $N_\star$. Models close to the equal-mass case show a deeper peak when $N_\star$ is rising than the high-μ models. Explanation is given in the text. Lower panel: the mean core number increases only slightly with $N_\star$. Disregarding the two highest μ, the number of minimum core particles is between 10 and 40.

determined, and then the corresponding time t' at which the same value was reached in the 5000-body model.

The ratio of these two times is a scalefactor, $\mathcal{S}_\mathrm{f}$, that should be also equal to the ratio of the relaxation times for the different $\mathcal{N}_\star$ before core rebounce:

$$\frac{t'}{t} \equiv \mathcal{S}_\mathrm{f} := \frac{\mathcal{N}'_\star \ln(\gamma \mathcal{N}_\star)}{\mathcal{N}_\star \ln(\gamma \mathcal{N}'_\star)}. \tag{15}$$

By repeating this procedure for each time-step and for each Lagrangian radius we get an $\mathcal{S}_\mathrm{f}$ that is plotted in the lower panel of Fig. 12. Before the core collapse, the time ratios show a remarkable constancy (disregarding the initial settling period), and the inner Lagrangian radii have a good agreement. The scalefactor in the constant pre-collapse range is $\mathcal{S}_\mathrm{f} = 1.675$ for this model. With the definition $\nu := \mathcal{N}'_\star/\mathcal{N}_\star$, a re-arrangement of equation (15) yields

$$\gamma = \left(\frac{\mathcal{N}_\star}{(\mathcal{N}'_\star)^{\mathcal{S}_\mathrm{f}/\nu}}\right)\left(\frac{\nu}{\mathcal{S}_\mathrm{f} - \nu}\right). \tag{16}$$

We computed the values of γ for each model using the data sets of $\mathcal{N}_\star = 2.5 \times 10^3$ and $\mathcal{N}'_\star = 5 \times 10^3$. The results are given in Table 4 and plotted in Fig. 13. The first two rows of the table define the μ-model, the third gives the scalefactor as determined from the figures analogue to 12, the fourth is the error measured from the widths of the fluctuating lines in the stable regime (horizontal part), the fifth is the outer exponent in equation (16) with $\nu = 2$ and the sixth is the resulting values of γ.

The comparison of the data sets '$2.5 \times 10^3 \rightarrow 5 \times 10^3$' provides a more accurate scalefactor than the other data sets with lower $\mathcal{N}_\star$, because they rest upon a higher statistical significance. Our set with $\mathcal{N}_\star = 10^4$ can be averaged over four runs only, and the 10^3-set is biased to low-$\mathcal{N}_\star$ physics.

Very small variations in $\mathcal{S}_\mathrm{f}$ cause large fluctuations in the two exponents of equation (16) and alter γ significantly; the formula is very sensitive to both, $\mathcal{S}_\mathrm{f}$ and ν. The error was computed as the difference of an 'upper' and a 'lower' γ that results from the thickness of the $\mathcal{S}_\mathrm{f}$-line.

As for different ν, we present another example illustrating the big variations when determining the Coulomb-γ. Table 5 shows the results for the equal-mass models using various particle numbers $\mathcal{N}_\star$ and $\mathcal{N}'_\star$. The $\mathcal{S}_\mathrm{f}$ shows a reasonable behaviour for different values of ν and conforms to the result by Giersz & Heggie (1994a) shown in the last column. The resulting γ, however, differs at least by a factor of 5.

The value $\gamma = 0.11$ mentioned above is actually found due to the comparison of N-body and Fokker–Planck simulations of equal-mass models (Giersz & Heggie 1994a, Fig. 5). From their N-body

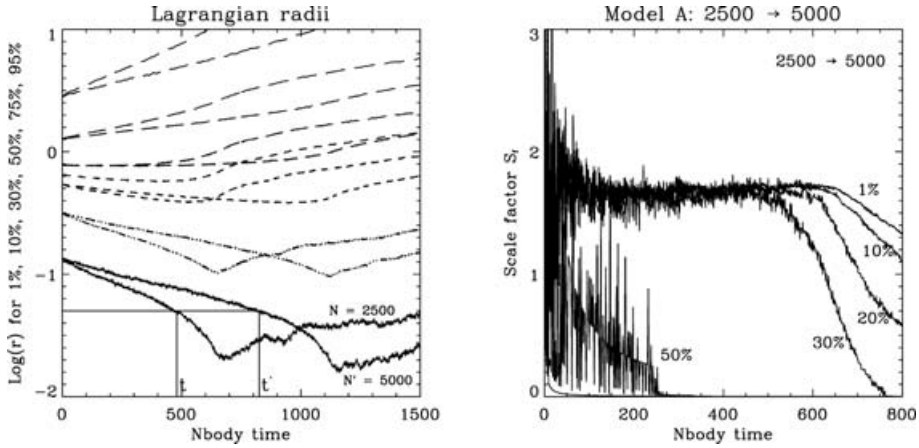

Figure 12. Upper panel: five selected Lagrangian radii of model A for $\mathcal{N}_\star = 2.5 \times 10^3$ and $\mathcal{N}'_\star = 5 \times 10^3$. Lower panel: scalefactor S_f for this model computed from the comparison of the Lagrangian radii.

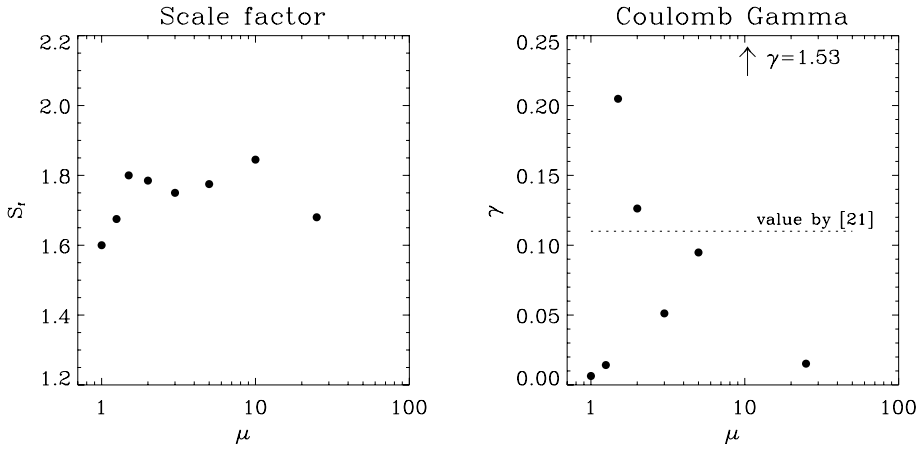

Figure 13. Upper panel: scalefactors measured from figures analogue to 12 for various μ. Lower panel: Coulomb-γ as determined from N-body simulations with different particle numbers from equation (16). The error bars are larger than the panel size.

Table 4. Scalefactors and values of γ for the models with different μ. The data were determined by comparing the data sets $N_\star = 2500$ and $N'_\star = 5000$, giving a particle ratio $\nu = 2$.

Model	A	B	C	D	E	F	G
μ	1.25	1.5	2.0	3.0	5.0	10.0	25.0
$\mathcal{S}_f$	1.675	1.800	1.785	1.750	1.775	1.845	1.680
$\Delta\mathcal{S}_f$	0.045	0.010	0.035	0.030	0.175	0.045	0.190
$\nu/(\mathcal{S}_f - \nu)$	−6.154	−10.00	−9.302	−8.000	−8.889	−12.903	−6.250
γ	0.0142	0.2048	0.1263	0.0512	0.0948	1.5321	0.0152

Table 5. Comparison of our equal-mass models with four different particle numbers and the N-body-analysis by Giersz & Heggie (1994a) in the last column.

Equal mass	$1000 \rightarrow 2500$	$1000 \rightarrow 5000$	$2500 \rightarrow 5000$	$2500 \rightarrow 10\,000$	Giersz & Heggie (1994a)
ν	2.5	5.0	2.0	4.0	4.0
$\mathcal{S}_f$	1.96	3.21	1.60	3.09	2.95
$\nu/(\mathcal{S}_f - \nu)$	−4.630	−2.793	−5.00	−4.396	−3.810
γ	0.028	0.018	0.006	0.044	0.098

simulations with particle numbers of $\mathcal{N}_\star = 500$ and $\mathcal{N}'_\star = 2000$ (their fig. 5), it is easy to extract an $\mathcal{S}_f = 2.95$ and get a $\gamma = 0.098$. For the same particle ratio, $\nu = 4.0$, we obtain a γ that is half of theirs (last two columns in Table 5). But our absolute particle numbers are five times larger. We can conclude from our analysis that the choice of $\mathcal{N}_\star$ and $\mathcal{N}'_\star$ essentially contributes to the Coulomb-γ.

Finally, we are left with a fair range of possible values for γ. An estimate indicates that γ ranges somewhere between 0.01 and 0.20. A similar range was given by Giersz & Heggie (1996) for the case of a power-law mass spectrum: $0.016 \lesssim \gamma \lesssim 0.26$.

9 VARIATIONS OF THE MASS FRACTION

So far, we have presented results on mass segregation for various values of μ. This section deals with three additional series, in which we alter the fraction of the heavy masses, q. Such kind of study has been discussed by Watters et al. (2000) with a Monte Carlo approach or by Inagaki & Wiyanto (1984), who simulated two-component clusters by means of the Fokker–Planck modelling. They fixed μ to 2.0 and investigated the core-collapse times as well as the achievement of equipartition. They showed that the evolution of the central potential in units of the half-mass relaxation time, $t_{\rm rh}$, for four different values of q is fastest when $q \approx 0.1$.

We present in this section the question whether equipartition can be achieved between the two components while segregation is on work and a comparison of the N-body data with the above mentioned literature.

We investigate the equipartition parameter

$$\xi = \frac{m_{\rm h}\sigma_2^2}{m_{\rm l}\sigma_1^2}, \tag{17}$$

which gives the ratio of the kinetic energies between the heavy and light stars in the core. At the start its value is about μ and heads for unity. When both mass species find a state of energy equipartition, $\xi = 1$ is reached, and we call the system equipartition stable (after Spitzer 1969), otherwise a $\xi_{\rm min}$ indicates the closest approach to it.

When examining a particular run, the data of ξ is very noisy, especially, for small-$\mathcal{N}_\star$ simulations. The main cause for this is the

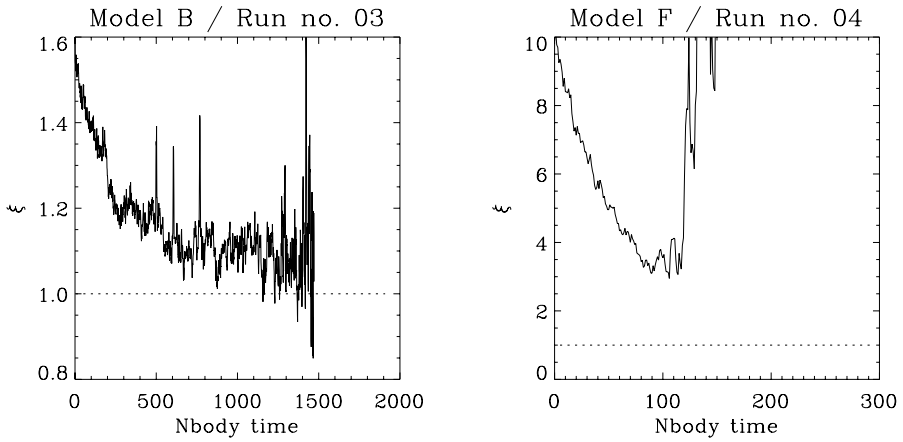

Figure 14. Equipartition parameter for two runs from model B (upper panel) and F (lower panel), respectively, containing 10 000 particles. The data were smoothed out with a smooth width $w = 5$ as described in Section 3.1.

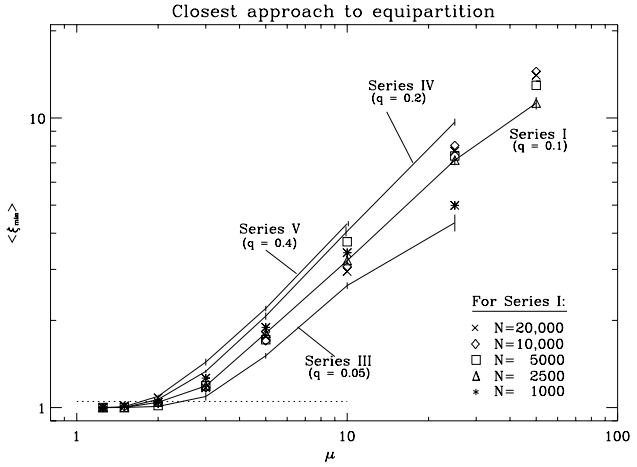

Figure 15. The averaged minimum of the equipartition parameter ξ for stars inside twice the core radius. When both mass components are in the equipartition, $\xi_{\rm min}$ equals 1. The solid lines connect the data points for $q = 0.4$ (series V), $q = 0.2$ (series IV), $q = 0.1$ (series I with triangles) and $q = 0.05$ (series III). These four simulation series were made with $\mathcal{N}_\star = 2.5 \times 10^3$ particles, and error bars are given for them. The dotted line is an arbitrary threshold for the equipartition stability at 1.05 as explained in the text.

small number of particles inside the core radius. For this reason, we decided to evaluate for the particles inside twice the core radius, and then apply the smoothing procedure of Section 3.1. We define $\xi_{\rm min} = 1$, if equation (17) drops below unity at any time during the evolution; otherwise we set it to the deepest peak. Fig. 14 shows an example for the parameter ξ from two models with $\mathcal{N}_\star = 104$. The B-model does reach equipartition at $t = 1157$, so $\xi_{\rm min}$ is set to 1; the F-model approaches to it down to $\xi_{\rm min} = 2.95$ at $t = 106$.

The average from all the runs particularly the values of $\xi_{\rm min}$ is denoted by $\langle \xi_{\rm min} \rangle$ and taken as the most reliable data for the model. The values of $\langle \xi_{\rm min} \rangle$ are plotted versus μ in Fig. 15. All the symbols belong to the series I with $q = 0.1$, but with a different particle number. The solid line connects the $\mathcal{N}_\star = 2.5 \times 10^3$ values (triangles). The additional series III ($q = 0.05$), IV ($q = 0.2$) and V ($q = 0.4$) are shown as solid lines. Error bars are given only for the four sets with $\mathcal{N}_\star = 2.5 \times 10^3$; they are smaller than the symbols in most cases.

As expected, the graphic shows that equipartition takes place for small values of μ, but when μ becomes significantly greater than 2, $\langle \xi_{\rm min} \rangle$ recedes from unity. At $\mu = 2$, about half of the individual runs with $q = 0.1$ did succeed to reach $\xi_{\rm min} = 1$, at least for a moment. Those runs, which did not find a state of full equipartition, tried to reduce the kinetic difference halfways to the core collapse, but then departed shortly after the closest approach.

Table 6. Values of μ at which $\xi_{\rm min} > 1.05$. Equipartition cannot be attained anymore. See the text for further details.

Series	q	$\mu_{\rm crit}$	
III	0.05	2.49	
I	0.10	2.03	2.032 ($\mathcal{N}_\star = 1000$) 2.048 ($\mathcal{N}_\star = 2500$) 2.197 ($\mathcal{N}_\star = 5000$) 2.111 ($\mathcal{N}_\star = 10k$) 1.762 ($\mathcal{N}_\star = 20k$)
IV	0.20	1.87	
V	0.40	1.75	

That figure provides a good basis for the judgement on equipartition stability. It is obvious that $\langle \xi_{\rm min} \rangle$ varies for different fractions of heavy masses, q: the less the amount of heavy masses in a cluster, the closer the equipartition is reached. This is consistent with the results by both Inagaki & Wiyanto (1984) and Watters et al. (2000). The latter explore an even wider range to very low values of q down to 0.0015 (their set 'B').

In order to check the stability border, we look now for a 'critical μ' at which equipartition stability is *not* given.

Instead of assuming that equipartition happens for $\langle \xi_{\rm min} \rangle = 1$, we will give a small tolerance for this and define the point of 'turning away' from equipartition at $\langle \xi_{\rm min} \rangle = 1.05$, as Watters et al. (2000) did. It is denoted by the dotted horizontal line in Fig. 15. By linear interpolation between the lower- and upper-next data point, one obtains that this threshold is exceeded at the points $\mu_{\rm crit}$ given in Table 6.

The value for series I was averaged from all simulation sets for different $\mathcal{N}_\star$. All values of $\langle \xi_{\rm min} \rangle$ are plotted in Fig. 16, and fitted for a direct comparison of the Monte Carlo results from Watters et al. (2000). The positions of our $\mu_{\rm crit}$ are marked by a small filled dot. The apparent difference for the line by Lightman & Fall (1978) is just because Watters et al. (2000) defined their fraction of heavy masses as $\hat{q} = \mathcal{M}_{\rm h}/\mathcal{M}_{\rm l}$, whereas we use $q = \mathcal{M}_{\rm h}/\mathcal{M}_{\rm cl}$ (see Section 2.1). The graphics and the results are consistent with each other and ease the comparison.

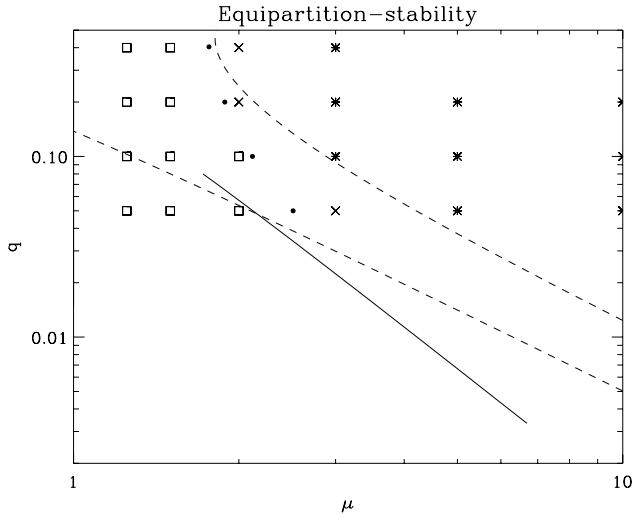

Figure 16. Closest approach to equipartition for the models in our parameter range of μ (mass ratio of heavy stars to light stars) and q (mass in heavy stars relative to total cluster mass, see also Fig. 1). The figure has been adjusted (symbols, axes and lines are accommodated as explained in the text) so that one can easily compare it with the results with those of Watters et al. (2000) (Fig. 5). The solid line is their stability criterion, equation (2); the straight dashed line is from Spitzer (1969) and the curved dashed line is from Lightman & Fall (1978).

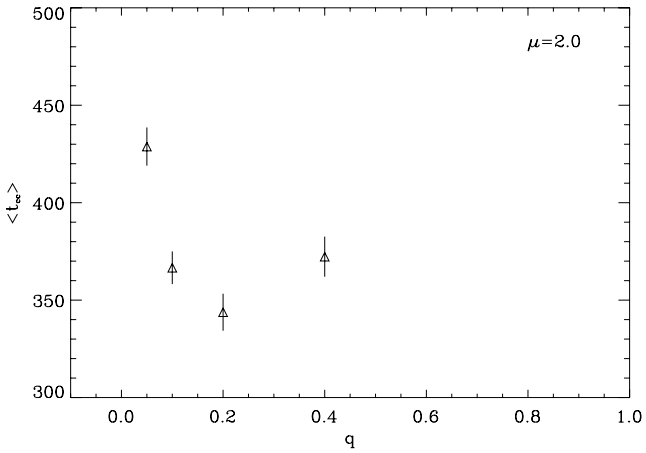

Figure 17. Core-collapse time $t_{\rm cc}$ as a function of q. The individual mass ratio, μ, was fixed to 2.0. The gas models by Bettwieser & Inagaki (1985) show a broad minimum for the core-collapse times in terms of the relaxation time. The value of q for fastest evolution is ≈0.1–0.2. The results of the N-body models for the four series are discussed in the text. The time on the vertical axis is given in N-body units.

Although we have four points for $\mu_{\rm crit}$ in order to check the equipartition boundary, they follow the theoretical function by Lightman & Fall (1978) in fair agreement.

The formula suggested by Watters et al. (2000) cannot be ruled out, because it is based on the models in a low-q regime, which is difficult to access with our N-body simulations. However, our experimental data show that the criterion by Spitzer (1969) for the stability boundary, appears too strong, especially at mass ratios μ close to 1.

$\mu_{\rm crit} \approx 2$ is the point which was already recognized as the transition of an equipartition-dominated and a gravothermal-dominated collapse (Section 5). Below $\mu_{\rm crit}$, the core collapse proceeds slower than the theory predicts, because equipartition governs the initial phase. When $\mu > \mu_{\rm crit}$, the gravothermal instability always wins the competition between the two effects. Before the thermal equilibrium can fully be achieved, the massive stars have already segregated to the centre and collapse independently from the light stars. With the total fraction q being high, the massive component appears almost self-gravitating and is decoupled from the beginning.

Bettwieser & Inagaki (1985) showed that there is an 'optimal' q that favours the collapse of a two-component system. If q is small, the collapse of the heavier component proceeds in the external field of the lighter stars, and the collapse time decreases rapidly. On the other hand, if q is very large, the amount of thermal energy contained in the core of the massive stars is so large that the core of the light ones cannot receive all the redundant energy. Hence the tendency to collapse is postponed, because the heat gained has to be dumped away into the halo and this process is slower than the tendency to equipartition (see also Lee 1995). Finally, the extreme cases $q \to 0$ and 1 approach the single-mass value for a negligible contribution of the heavy and light component, respectively. This is the reason why the core-collapse time attains a minimum at a certain fraction of the heavier stars (Bettwieser & Inagaki 1985). The N-body models confirm this (Fig. 17).

10 CONCLUSIONS

We have studied mass segregation and equipartition in idealized star clusters containing two mass components. The results provide potential insight into the evolution of young star clusters, dynamics of star forming regions and the degree of initial segregation which is needed to match the observations. Also, this study is of theoretical interest to check the classical ideas on the equipartition and the thermodynamic behaviour of self-gravitating systems.

The parameter space was widely analysed for both parameters using Plummer models: the ratio of individual star masses, $\mu = m_{\rm h}/m_{\rm l}$, that was varied from 1.25 to 50; and the fraction of the total heavy masses, $q = \mathcal{M}_{\rm h}/\mathcal{M}_{\rm cl}$, that was chosen to be 0.05, 0.1, 0.2, or 0.4. We also directed our attention to the value $q = 0.1$, which was proved by Inagaki & Wiyanto (1984) to exhibit the fastest evolution time. For this fraction, we modelled different particle numbers, with $\mathcal{N}_\star$ ranging from 10^3 to 2×10^4. For all other cases, we used a particle number of $\mathcal{N}_\star = 2.5 \times 10^3$. The statistical significance of the data was considerably improved by ensemble averages. A large number of physically equivalent runs differing just by a random seed for an initial set-up was performed, and the data base was gathered for an overall average.

For the first time, we have empirically checked the borders between an equipartition stable and unstable configuration (Spitzer 1969) with the accurate, direct N-body method. His criterion involves the parameters q and μ and is given in equation (1). Moreover, we determined the ranges of the longest and shortest core-collapse time by comparing different initial set-ups of the particles.

From the results of our simulations we draw the following conclusions on the global cluster evolution.

(i) The evolution of a self-gravitating system with two mass components depends strongly on the ratio of the individual masses, $\mu = m_{\rm h}/m_{\rm l}$. For $q = 0.1$, when μ is larger than ≈ 2, the heavy masses fall to the centre and reduce the relaxation time proportional to $1/\mu$. Subsidiary, the core-collapse time is shortened in the same way (Fig. 5). Smaller values of μ go into the equipartition which slows down the evolution. Large values of μ give rise to a small number of heavy particles, and the situation turns into a process of dynamical friction.

(ii) There is a competition between equipartition of energies and gravothermal instability. If μ is close to unity, equipartition hinders the gravothermal collapse in the initial phase, but will never prevent it. As the heavy stars congregate in the central regions, they decouple from the light component and perform their own collapse. When μ exceeds a critical value of about 2, equipartition can never be achieved (Fig. 15).

(iii) The boundary between the stable and unstable regimes is close to the theory by Lightman & Fall (1978) when q is $\gtrsim$0.2. For q lower than $\approx$0.1, other works on the equipartition (Watters et al. 2000) seem to show a better agreement, but it is difficult to assess their range with N-body simulations because the absolute number of very heavy particles is too low in our standard $N_\star$ (Fig. 16). When q becomes larger than 0.1, the criterion given by Spitzer (1969) appears too strong, and his theory fails. According to equation (1), no equipartition should be possible at all, while our models as well as the Monte Carlo simulations by Watters et al. (2000) show the contrary. The cause is probably that Spitzer assumed a global equilibrium when deriving the analytical formulae. His basic ideas on the processes, however, are still in fair accordance with our results.

(iv) Segregation proceeds on the relaxation time-scale simultaneously with the evolution of the cluster. The maximum level of segregation is attained when the core has collapsed and began to expand. Then, the mass shells in the cluster have also adjusted to a stable balance of an ingoing and outgoing mass flux (Fig. 6). After the core collapse, the degree of stratification remains constant.

(v) The escape rate shows two branches along the μ-axis indicating two different mechanisms being on work (Fig. 9e). For mass ratios resembling the equal-mass case, the escape seems to be governed by evaporational effects in the pre-collapse phase. Since the core-collapse time decreases for a moderately rising μ, evaporation does not advance far, so that the mass loss is also reduced. For high values of μ ($>$3), we believe that escapes are rather a matter of ejections; the very massive particles distribute their kinetic energy to a large number of stars, and the escape rate increases roughly with μ. The details of these processes, however, need more analysis tracing the path of the escapers or a countercheck with other simulation methods. As for the equal-mass case, the escape rate is consistent with other N-body simulations (Wielen 1975; Giersz & Heggie 1994a; Baumgardt, Hut & Heggie 2002).

(vi) Light masses play an important role in the heat transfer from the core to the halo. Even a small fraction of them moderates the heat flux between the central source and the outer sink. The 'optimal' fraction q of heavy to light stars is about 0.15–0.20 in accord with the previous results from gaseous models (Fig. 17).

Our results gained with the N-body method confirm previous simulations with other techniques (gas models, Monte Carlo), but also reveal hidden effects like the small 'deceleration' of the gravothermal collapse due to the equipartition. Further astrophysical assumptions are likely to alter the results, e.g. the introduction of primordial binaries in various fractions, a tidal field that accelerates the collapse as well as the dissolution of clusters, or the rotation. Multiple mass components or a continuous spectrum make the analysis more complex but are important for the understanding of the observations. Our variation of μ can principally be generalized by merging into a multimass model, but care has to be taken when defining the parameters. The new parameters appearing for the models are to be checked, e.g. the slope of the initial mass function (if a power law is assumed), and how the ratio of the highest mass to the mean mass, $m_{\max}/\langle m\rangle$, influences the segregation.

ACKNOWLEDGMENTS

This work has been supported by Sonderforschungsbereich (SFB) 439 (subproject A5) of German Science Foundation (DFG) at the University of Heidelberg. Here, the computations here were carried out at the CRAY T3E parallel computer at the Hochleistungsrechenzentrum in Stuttgart.[1]

The work of PAS has been supported in the framework of the Third Level Agreement between the DFG and the IAC (Instituto de Astrofísica de Canarias). PAS thanks Marc Freitag for both fruitful discussions and very useful comments for the elaboration and redaction of the text of the work, settled during his visit in 2006 February to the Institute of Astronomy in Cambridge. This was possible on the account of an invitation by Marc Freitag.

REFERENCES

Aarseth S. J., Henon M., Wielen R., 1974, A&A, 37, 183
Baumgardt H., 2001, MNRAS, 325, 1323
Baumgardt H., Hut P., Heggie D. C., 2002, MNRAS, 336, 1069
Bettwieser E., Inagaki S., 1985, MNRAS, 213, 473
Bonnell I. A., Davies M. B., 1998, MNRAS, 295, 691
Cohn H., 1980, ApJ, 242, 765
Drukier G. A., Cohn H. N., Lugger P. M., Yong H., 1999, ApJ, 518, 233
Fregeau J. M., Joshi K. J., Portegies Zwart S. F., Rasio F. A., 2002, ApJ, 570, 171
Giersz M., Heggie D. C., 1994a, MNRAS, 268, 257
Giersz M., Heggie D. C., 1994b, MNRAS, 270, 298
Giersz M., Heggie D. C., 1996, MNRAS, 279, 1037
Goodman J., 1984, ApJ, 280, 298
Goodman J., 1987, ApJ, 313, 576
Ghűrkan M. A., Freitag M., Rasio F. A., 2004, ApJ, 604, 632
Hénon M., 1965, Annales d'Astrophysique, 28, 62
Heggie D. C., Mathieu R. D., 1986, in Hut P., McMillan S. L. W., eds, Lecture Notes in Physics Vol. 267, The Use of Supercomputers in Stellar Dynamics. Springer-Verlag, Berlin, p. 233
Hénon M., 1969, A&A, 2, 151
Hénon M., 1973, in Contopoulos G., Henon M., Lynden-Bell D., eds, Saas-Fee Advanced Course 3, Dynamical Structure and Evolution of Stellar Systems. Geneva Obs., Sauverny, Dynamical Structure and Evolution of Stellar Systems, p. 183
Hénon M., 1975, in Hayli A., ed., IAU Symp. 69, Dynamics of Stellar Systems. Reidel, Dordrecht, p. 133
Hillenbrand L. A., Hartmann L. W., 1998, ApJ, 492, 540
Inagaki S., Wiyanto P., 1984, PASJ, 36, 391
Joshi K. J., Rasio F. A., Portegies Zwart S., 2000, ApJ, 540, 969
Kim S. S., Lee H. M., Goodman J., 1998, ApJ, 495, 786
Lee H. M., 1995, MNRAS, 272, 605
Lightman A. P., Fall S. M., 1978, ApJ, 221, 567
Makino J., 1996, ApJ, 471, 796
Marchant A. B., Shapiro S. L., 1980, ApJ, 239, 685
McCaughrean M. J., Stauffer J. R., 1994, AJ, 108, 1382
McMillan S. L. W., Lightman A. P., Cohn H., 1981, ApJ, 251, 436
Meylan G., Heggie D. C., 1997, A&AR, 8, 1
Portegies Zwart S. F., McMillan S. L. W., 2000, ApJ, 528, L17
Quinlan G. D., 1996, New Astron., 1, 255
Raboud D., Mermilliod J.-C., 1998, A&A, 333, 897
Shapiro S. L., 1977, ApJ, 217, 281
Spitzer L. J., 1969, ApJ, 158, L139
Spitzer L., 1987, Dynamical Evolution of Globular clusters. Princeton Univ. Press, Princeton, NJ
Spitzer L. J., Hart M. H., 1971, ApJ, 166, 483
Spitzer L., Shull J. M., 1975, ApJ, 200, 339
Spurzem R., Aarseth S. J., 1996, MNRAS, 282, 19

[1] http://www.hlrs.de/

Spurzem R., Takahashi K., 1995, MNRAS, 272, 772
Stodołkiewicz J. S., 1982, Acta Astron., 32, 63
Takahashi K., 1993, PASJ, 45, 233
Takahashi K., 1995, PASJ, 47, 561
von Hoerner S., 1960, Zeitschrift fur Astrophysics, 50, 184
Watters W. A., Joshi K. J., Rasio F. A., 2000, ApJ, 539, 331
Wielen R., 1975, in Hayli A., ed., IAU Symp. 69, Dynamics of the Solar Systems. Reidel, Dordrecht, p. 119

APPENDIX A: DATA TABLES

The following Tables A1–A14 contain the mean values of the simulations of star clusters and are organized as follows. The title specifies the series, q and particle number. The columns of the tables are defined as follows.

(i) Column 1: model name and μ.

(ii) Column 2: $\langle t_{\rm cc}\rangle$, mean core-collapse time.

(iii) Column 3: $\langle \Phi_{\rm min}\rangle$, depth of central potential.

(iv) Column 4: $\langle r_{\rm c}\rangle$, mean core radius in the moment of core bounce.

(v) Column 5: $\langle \mathcal{N}_{\rm c}\rangle$, number of particles in the core at the time of smallest core radius.

(vi) Column 6: $\langle \xi_{\rm min}\rangle$, mean of the closest approach to equipartition.

(vii) Column 7: $\langle \mathcal{N}_{\rm esc}\rangle$, number of escaped stars until core-collapse time.

(viii) Column 8: $\langle E_{\rm esc}\rangle$, mean energy of escapers.

Table A1. Equal mass: $\mathcal{N}_\star = 1000$.

Model	$\langle t_{\rm cc}\rangle$	$\langle \Phi_{\rm min}\rangle$	$\langle r_{\rm c}\rangle$	$\langle \mathcal{N}_{\rm c}\rangle$	$\langle \xi_{\rm min}\rangle$	$\langle \mathcal{N}_{\rm esc}\rangle$	$\langle E_{\rm esc}\rangle$
EQMASS01	345.8 ± 5.2	-4.72 ± 0.10	0.0208 ± 0.0020	11.2 ± 0.4	—	26.6 ± 1.1	0.88 ± 0.18

Table A2. Equal mass: $\mathcal{N}_\star = 2500$.

Model	$\langle t_{\rm cc}\rangle$	$\langle \Phi_{\rm min}\rangle$	$\langle r_{\rm c}\rangle$	$\langle \mathcal{N}_{\rm c}\rangle$	$\langle \xi_{\rm min}\rangle$	$\langle \mathcal{N}_{\rm esc}\rangle$	$\langle E_{\rm esc}\rangle$
EQMASS02	716.0 ± 12.0	-6.02 ± 0.16	0.0086 ± 0.0006	14.8 ± 0.8	—	64.2 ± 3.1	0.89 ± 0.24

Table A3. Equal mass: $\mathcal{N}_\star = 5000$.

Model	$\langle t_{\rm cc}\rangle$	$\langle \Phi_{\rm min}\rangle$	$\langle r_{\rm c}\rangle$	$\langle \mathcal{N}_{\rm c}\rangle$	$\langle \xi_{\rm min}\rangle$	$\langle \mathcal{N}_{\rm esc}\rangle$	$\langle E_{\rm esc}\rangle$
EQMASS05	1210.2 ± 10.6	-7.58 ± 0.27	0.0045 ± 0.0003	17.7 ± 0.8	—	117.1 ± 5.0	0.71 ± 0.26

Table A4. Equal mass: $\mathcal{N}_\star = 10\,000$.

Model	$\langle t_{\rm cc}\rangle$	$\langle \Phi_{\rm min}\rangle$	$\langle r_{\rm c}\rangle$	$\langle \mathcal{N}_{\rm c}\rangle$	$\langle \xi_{\rm min}\rangle$	$\langle \mathcal{N}_{\rm esc}\rangle$	$\langle E_{\rm esc}\rangle$
EQMASS10	2312.9 ± 34.7	-8.75 ± 0.47	0.0025 ± 0.0004	21.3 ± 2.2	—	256.3 ± 7.1	2.55 ± 1.43

Table A5. Series I: $q = 0.1$, $\mathcal{N}_\star = 1000$.

Model (μ)	$\langle t_{\rm cc}\rangle$	$\langle \Phi_{\rm min}\rangle$	$\langle r_{\rm c}\rangle$	$\langle \mathcal{N}_{\rm c}\rangle$	$\langle \xi_{\rm min}\rangle$	$\langle \mathcal{N}_{\rm esc}\rangle$	$\langle E_{\rm esc}\rangle$
A (1.25)	309.1 ± 5.8	-4.60 ± 0.11	0.0206 ± 0.0009	11.1 ± 0.4	1.002 ± 0.002	22.9 ± 1.2	0.70 ± 0.17
B (1.5)	256.0 ± 5.1	-4.10 ± 0.07	0.0275 ± 0.0011	11.7 ± 0.3	1.011 ± 0.005	18.4 ± 1.1	0.70 ± 0.11
C (2.0)	162.6 ± 3.5	-3.52 ± 0.04	0.0400 ± 0.0016	12.0 ± 0.5	1.043 ± 0.010	9.5 ± 0.5	0.78 ± 0.24
D (3.0)	86.1 ± 2.1	-3.27 ± 0.06	0.0596 ± 0.0026	12.0 ± 0.6	1.264 ± 0.033	4.8 ± 0.4	1.02 ± 0.26
E (5.0)	45.8 ± 1.4	-3.24 ± 0.06	0.0797 ± 0.0040	12.5 ± 0.8	1.892 ± 0.071	0.0 ± 0.0	0.00 ± 0.00
F (10.0)	25.4 ± 0.9	-3.65 ± 0.08	0.0954 ± 0.0039	12.1 ± 0.7	3.426 ± 0.187	4.1 ± 0.4	1.28 ± 0.33
G (25.0)	18.0 ± 0.7	-4.72 ± 0.12	0.0785 ± 0.0030	7.3 ± 0.4	4.992 ± 0.237	12.9 ± 0.2	1.09 ± 0.12

Table A6. Series I: $q = 0.1$, $\mathcal{N}_\star = 2500$.

Model (μ)	$\langle t_{\rm cc}\rangle$	$\langle \Phi_{\rm min}\rangle$	$\langle r_{\rm c}\rangle$	$\langle \mathcal{N}_{\rm c}\rangle$	$\langle \xi_{\rm min}\rangle$	$\langle \mathcal{N}_{\rm esc}\rangle$	$\langle E_{\rm esc}\rangle$
A (1.25)	677.8 ± 8.1	-5.51 ± 0.12	0.0100 ± 0.0005	15.9 ± 0.7	1.000 ± 0.000	61.3 ± 2.0	0.77 ± 0.27
B (1.5)	558.4 ± 8.8	-5.02 ± 0.11	0.0137 ± 0.0006	15.9 ± 0.8	1.001 ± 0.000	45.2 ± 2.2	0.55 ± 0.14
C (2.0)	366.6 ± 8.4	-4.06 ± 0.11	0.0207 ± 0.0011	14.4 ± 1.0	1.043 ± 0.028	24.9 ± 1.6	1.18 ± 0.28
D (3.0)	180.1 ± 2.9	-3.50 ± 0.10	0.0336 ± 0.0019	16.2 ± 2.3	1.188 ± 0.017	9.7 ± 0.6	0.70 ± 0.12
E (5.0)	86.1 ± 3.3	-3.17 ± 0.10	0.0567 ± 0.0043	17.0 ± 1.4	1.807 ± 0.056	7.3 ± 0.8	1.43 ± 0.27
F (10.0)	40.2 ± 2.0	-3.45 ± 0.15	0.0811 ± 0.0054	19.9 ± 1.8	3.218 ± 0.086	8.0 ± 0.7	0.89 ± 0.12
G (25.0)	21.8 ± 1.1	-4.11 ± 0.18	0.0905 ± 0.0048	19.7 ± 1.7	7.150 ± 0.282	12.4 ± 0.9	0.86 ± 0.15
H (50.0)	17.9 ± 1.1	-6.16 ± 0.36	0.0792 ± 0.0039	11.7 ± 1.0	11.245 ± 0.556	25.2 ± 2.6	0.98 ± 0.15

Table A7. Series I: $q = 0.1, \mathcal{N}_\star = 5000$.

Model (μ)	$\langle t_{\rm cc}\rangle$	$\langle \Phi_{\rm min}\rangle$	$\langle r_{\rm c}\rangle$	$\langle \mathcal{N}_{\rm c}\rangle$	$\langle \xi_{\rm min}\rangle$	$\langle \mathcal{N}_{\rm esc}\rangle$	$\langle E_{\rm esc}\rangle$
A (1.25)	1183.7 ± 17.7	-6.92 ± 0.18	0.0055 ± 0.0004	19.8 ± 0.7	1.000 ± 0.000	103.9 ± 5.0	0.44 ± 0.13
B (1.5)	993.8 ± 10.3	-5.85 ± 0.12	0.0071 ± 0.0003	16.9 ± 1.0	1.000 ± 0.000	76.9 ± 3.2	0.57 ± 0.14
C (2.0)	642.6 ± 4.4	-4.62 ± 0.20	0.0117 ± 0.0011	15.8 ± 1.4	1.016 ± 0.008	38.0 ± 1.9	0.47 ± 0.09
D (3.0)	331.5 ± 11.6	-3.72 ± 0.08	0.0204 ± 0.0013	16.8 ± 1.4	1.189 ± 0.037	19.3 ± 2.6	1.08 ± 0.45
E (5.0)	157.9 ± 6.3	-3.36 ± 0.12	0.0302 ± 0.0025	14.9 ± 1.1	1.715 ± 0.039	14.2 ± 1.9	1.38 ± 0.27
F (10.0)	64.3 ± 3.5	-3.11 ± 0.09	0.0742 ± 0.0055	29.4 ± 2.8	3.738 ± 0.256	10.4 ± 1.0	2.17 ± 1.01
G (25.0)	33.3 ± 0.9	-4.43 ± 0.34	0.0842 ± 0.0025	29.1 ± 1.4	7.394 ± 0.214	17.7 ± 1.2	0.97 ± 0.09
H (50.0)	22.4 ± 0.7	-5.64 ± 0.43	0.0789 ± 0.0089	26.2 ± 3.5	12.962 ± 0.358	25.8 ± 3.1	1.15 ± 0.18

Table A8. Series I: $q = 0.1, \mathcal{N}_\star = 10\,000$.

Model (μ)	$\langle t_{\rm cc}\rangle$	$\langle \Phi_{\rm min}\rangle$	$\langle r_{\rm c}\rangle$	$\langle \mathcal{N}_{\rm c}\rangle$	$\langle \xi_{\rm min}\rangle$	$\langle \mathcal{N}_{\rm esc}\rangle$	$\langle E_{\rm esc}\rangle$
A (1.25)	2169.9 ± 24.7	-8.35 ± 0.52	0.0027 ± 0.0003	20.0 ± 2.7	1.000 ± 0.000	227.3 ± 3.9	0.40 ± 0.11
B (1.5)	1886.8 ± 8.6	-7.05 ± 0.39	0.0042 ± 0.0001	20.8 ± 1.0	1.008 ± 0.006	172.3 ± 9.3	0.35 ± 0.06
C (2.0)	1218.0 ± 20.1	-5.85 ± 0.37	0.0053 ± 0.0007	15.8 ± 1.8	1.035 ± 0.014	91.3 ± 4.3	0.78 ± 0.17
D (3.0)	595.1 ± 8.5	-3.97 ± 0.17	0.0107 ± 0.0010	15.0 ± 1.9	1.170 ± 0.024	35.3 ± 3.4	1.03 ± 0.27
E (5.0)	277.6 ± 9.7	-4.18 ± 0.32	0.0235 ± 0.0004	19.8 ± 1.4	1.700 ± 0.029	19.3 ± 1.4	0.63 ± 0.08
F (10.0)	123.5 ± 2.1	-3.80 ± 0.31	0.0351 ± 0.0055	22.3 ± 3.9	3.065 ± 0.108	25.5 ± 2.0	1.19 ± 0.04
G (25.0)	52.4 ± 2.3	-4.92 ± 0.42	0.0741 ± 0.0108	36.8 ± 6.1	8.040 ± 0.440	29.0 ± 2.9	2.05 ± 0.82
H (50.0)	37.5 ± 0.6	-6.82 ± 0.95	0.0894 ± 0.0059	47.8 ± 8.9	14.478 ± 0.859	42.3 ± 5.3	0.93 ± 0.28

Table A9. Series I: $q = 0.1, \mathcal{N}_\star = 20\,000$.

Model (μ)	$\langle t_{\rm cc}\rangle$	$\langle \Phi_{\rm min}\rangle$	$\langle r_{\rm c}\rangle$	$\langle \mathcal{N}_{\rm c}\rangle$	$\langle \xi_{\rm min}\rangle$	$\langle \mathcal{N}_{\rm esc}\rangle$	$\langle E_{\rm esc}\rangle$
A (1.25)	3859.0 ± 00.0	-8.62 ± 0.00	0.0021 ± 0.0000	33.0 ± 0.0	1.000 ± 0.000	422.0 ± 0.0	0.52 ± 0.00
B (1.5)	3318.0 ± 0.0	-9.09 ± 0.00	0.0030 ± 0.0000	36.0 ± 0.0	1.016 ± 0.000	292.0 ± 0.0	0.79 ± 0.00
C (2.0)	2236.0 ± 0.0	-5.64 ± 0.00	0.0044 ± 0.0000	23.0 ± 0.0	1.081 ± 0.000	140.0 ± 0.0	0.34 ± 0.00
D (3.0)	1094.0 ± 0.0	-3.84 ± 0.00	0.0114 ± 0.0000	34.0 ± 0.0	1.170 ± 0.000	55.0 ± 0.0	0.56 ± 0.00
E (5.0)	608.0 ± 0.0	-4.21 ± 0.00	0.0103 ± 0.0000	16.0 ± 0.0	1.770 ± 0.000	65.0 ± 0.0	2.82 ± 0.00
F (10.0)	213.0 ± 0.0	-3.70 ± 0.00	0.0241 ± 0.0000	24.0 ± 0.0	2.950 ± 0.000	38.0 ± 0.0	1.34 ± 0.00
G (25.0)	78.0 ± 0.0	-4.95 ± 0.00	0.0863 ± 0.0000	88.0 ± 0.0	7.680 ± 0.000	30.0 ± 0.0	1.41 ± 0.00
H (50.0)	48.5 ± 0.0	-7.92 ± 0.00	0.0447 ± 0.0000	25.0 ± 0.0	14.046 ± 0.000	48.0 ± 0.0	0.78 ± 0.00

Table A10. Series II: $q = 0.1, \mathcal{N}_\star = 2500$, INS.

Model (μ)	$\langle t_{\rm cc}\rangle$	$\langle \Phi_{\rm min}\rangle$	$\langle r_{\rm c}\rangle$	$\langle \mathcal{N}_{\rm c}\rangle$	$\langle \xi_{\rm min}\rangle$	$\langle \mathcal{N}_{\rm esc}\rangle$	$\langle E_{\rm esc}\rangle$
A (1.25)	623.9 ± 11.1	-5.64 ± 0.10	0.0098 ± 0.0005	15.2 ± 0.5	—	57.5 ± 2.8	0.89 ± 0.22
B (1.5)	501.5 ± 9.1	-5.05 ± 0.10	0.0133 ± 0.0008	14.4 ± 0.8	—	42.0 ± 2.5	1.30 ± 0.56
C (2.0)	304.4 ± 8.0	-4.09 ± 0.12	0.0225 ± 0.0018	15.2 ± 1.0	—	16.9 ± 1.1	0.35 ± 0.18
D (3.0)	139.4 ± 4.6	-3.51 ± 0.07	0.0330 ± 0.0023	13.5 ± 0.9	—	8.5 ± 0.9	0.15 ± 0.11
E (5.0)	73.6 ± 3.0	-3.51 ± 0.08	0.0437 ± 0.0026	12.3 ± 0.8	—	8.4 ± 0.8	1.43 ± 0.40
F (10.0)	32.4 ± 1.7	-3.58 ± 0.13	0.0722 ± 0.0059	16.3 ± 1.9	—	5.9 ± 0.8	1.01 ± 0.29
G (25.0)	18.3 ± 0.9	-5.28 ± 0.33	0.0845 ± 0.0070	16.3 ± 2.9	—	13.6 ± 1.5	0.78 ± 0.11
H (50.0)	15.2 ± 0.9	-5.52 ± 0.27	0.0892 ± 0.0050	13.9 ± 1.4	—	25.7 ± 2.2	0.82 ± 0.10

Table A11. Series II: $q = 0.1, \mathcal{N}_\star = 2500$, OUT.

Model (μ)	$\langle t_{\rm cc}\rangle$	$\langle \Phi_{\rm min}\rangle$	$\langle r_{\rm c}\rangle$	$\langle \mathcal{N}_{\rm c}\rangle$	$\langle \xi_{\rm min}\rangle$	$\langle \mathcal{N}_{\rm esc}\rangle$	$\langle E_{\rm esc}\rangle$
A (1.25)	673.7 ± 8.6	-6.08 ± 0.16	0.0088 ± 0.0004	14.8 ± 0.6	—	61.4 ± 2.5	1.03 ± 0.41
B (1.5)	646.1 ± 11.3	-5.12 ± 0.14	0.0129 ± 0.0008	17.1 ± 0.9	—	50.1 ± 2.5	0.66 ± 0.14
C (2.0)	508.5 ± 10.8	-4.16 ± 0.12	0.0227 ± 0.0014	18.2 ± 1.2	—	32.6 ± 1.6	1.77 ± 0.42
D (3.0)	304.1 ± 7.3	-3.23 ± 0.05	0.0476 ± 0.0026	24.8 ± 1.8	—	13.0 ± 0.8	1.10 ± 0.30
E (5.0)	153.7 ± 4.7	-2.98 ± 0.06	0.0756 ± 0.0042	29.6 ± 2.8	—	8.5 ± 0.6	1.40 ± 0.32
F (10.0)	92.7 ± 3.0	-3.23 ± 0.08	0.0892 ± 0.0033	23.8 ± 1.6	—	10.0 ± 0.9	2.17 ± 0.47
G (25.0)	52.5 ± 1.5	-4.58 ± 0.27	0.0857 ± 0.0037	17.5 ± 1.2	—	17.0 ± 1.6	1.76 ± 0.26
H (50.0)	47.6 ± 2.3	-6.86 ± 0.29	0.0664 ± 0.0032	9.7 ± 0.7	—	32.0 ± 2.8	1.94 ± 0.32

Table A12. Series III: $q = 0.05, \mathcal{N}_\star = 2500$.

Model (μ)	$\langle t_{\rm cc}\rangle$	$\langle\Phi_{\rm min}\rangle$	$\langle r_{\rm c}\rangle$	$\langle\mathcal{N}_{\rm c}\rangle$	$\langle\xi_{\rm min}\rangle$	$\langle\mathcal{N}_{\rm esc}\rangle$	$\langle E_{\rm esc}\rangle$
K (1.25)	689.3 ± 7.8	-5.88 ± 0.21	0.0094 ± 0.0005	16.0 ± 0.6	1.000 ± 0.000	60.7 ± 2.5	0.53 ± 0.12
L (1.5)	605.3 ± 11.8	-5.19 ± 0.19	0.0140 ± 0.0009	17.2 ± 0.8	1.001 ± 0.000	51.0 ± 2.7	0.61 ± 0.16
M (2.0)	428.8 ± 9.8	-3.89 ± 0.11	0.0264 ± 0.0022	19.2 ± 1.4	1.009 ± 0.008	25.8 ± 1.7	0.82 ± 0.28
N (3.0)	219.3 ± 7.4	-3.20 ± 0.06	0.0443 ± 0.0028	19.5 ± 1.6	1.092 ± 0.034	9.3 ± 1.1	0.85 ± 0.27
P (5.0)	96.1 ± 4.5	-3.07 ± 0.06	0.0672 ± 0.0046	23.6 ± 2.4	1.510 ± 0.034	4.3 ± 0.7	1.60 ± 0.54
Q (10.0)	44.9 ± 1.4	-3.34 ± 0.11	0.0896 ± 0.0053	23.5 ± 2.4	2.638 ± 0.068	4.2 ± 0.6	1.06 ± 0.19
R (25.0)	27.6 ± 1.2	-4.53 ± 0.21	0.0903 ± 0.0046	19.0 ± 1.9	4.348 ± 0.290	9.0 ± 1.4	1.37 ± 0.44

Table A13. Series IV: $q = 0.2, \mathcal{N}_\star = 2500$.

Model (μ)	$\langle t_{\rm cc}\rangle$	$\langle\Phi_{\rm min}\rangle$	$\langle r_{\rm c}\rangle$	$\langle\mathcal{N}_{\rm c}\rangle$	$\langle\xi_{\rm min}\rangle$	$\langle\mathcal{N}_{\rm esc}\rangle$	$\langle E_{\rm esc}\rangle$
T (1.25)	657.1 ± 11.0	-5.88 ± 0.17	0.0102 ± 0.0006	15.2 ± 0.9	1.001 ± 0.000	62.5 ± 2.6	0.81 ± 0.21
U (1.5)	549.4 ± 7.6	-5.00 ± 0.14	0.0134 ± 0.0009	14.6 ± 0.8	1.000 ± 0.002	49.5 ± 2.7	1.17 ± 0.28
V (2.0)	343.8 ± 9.5	-4.51 ± 0.11	0.0166 ± 0.0011	12.3 ± 0.6	1.067 ± 0.012	26.7 ± 2.2	1.04 ± 0.35
W (3.0)	174.0 ± 3.9	-3.87 ± 0.11	0.0244 ± 0.0020	11.8 ± 0.8	1.334 ± 0.016	16.9 ± 1.3	0.61 ± 0.04
X (5.0)	86.3 ± 2.2	-3.55 ± 0.09	0.0391 ± 0.0028	12.0 ± 0.9	2.069 ± 0.059	13.9 ± 0.8	0.81 ± 0.08
Y (10.0)	48.6 ± 2.4	-3.97 ± 0.16	0.0564 ± 0.0041	11.9 ± 1.0	4.063 ± 0.161	21.1 ± 1.6	1.06 ± 0.11
Z (25.0)	22.7 ± 1.0	-4.72 ± 0.24	0.0869 ± 0.0049	15.5 ± 1.6	9.676 ± 0.267	30.1 ± 1.97	0.74 ± 0.07

Table A14. Series V: $q = 0.4, \mathcal{N}_\star = 2500$.

Model (μ)	$\langle t_{\rm cc}\rangle$	$\langle\Phi_{\rm min}\rangle$	$\langle r_{\rm c}\rangle$	$\langle\mathcal{N}_{\rm c}\rangle$	$\langle\xi_{\rm min}\rangle$	$\langle\mathcal{N}_{\rm esc}\rangle$	$\langle E_{\rm esc}\rangle$
T′ (1.25)	639.7 ± 9.9	-5.79 ± 0.16	0.0092 ± 0.0007	14.0 ± 0.8	1.000 ± 0.000	63.0 ± 2.4	0.68 ± 0.13
U′ (1.5)	523.2 ± 8.2	-5.24 ± 0.12	0.0117 ± 0.0006	14.4 ± 0.8	1.007 ± 0.003	51.4 ± 2.7	0.81 ± 0.22
V′ (2.0)	372.3 ± 10.3	-4.95 ± 0.15	0.0149 ± 0.0007	13.3 ± 0.6	1.094 ± 0.013	42.3 ± 2.9	0.85 ± 0.24
W′ (3.0)	212.8 ± 4.3	-4.27 ± 0.10	0.0195 ± 0.0014	11.3 ± 0.6	1.436 ± 0.039	38.7 ± 2.4	0.57 ± 0.03
X′ (5.0)	130.7 ± 4.0	-4.19 ± 0.14	0.0274 ± 0.0015	10.4 ± 0.6	2.200 ± 0.047	43.7 ± 2.9	0.81 ± 0.05
Y′ (10.0)	66.8 ± 2.5	-4.26 ± 0.12	0.0440 ± 0.0026	9.9 ± 0.5	4.316 ± 0.087	50.9 ± 3.5	0.88 ± 0.05

APPENDIX B: *N*-BODY-UNITS AND TIME-SCALES

Dimensionless units, so-called '*N*-body units', were used throughout the calculations. They are obtained when setting the gravitational constant G and the initial total cluster mass $\mathcal{M}_{\rm cl}$ equal to 1, and the initial total energy E to $-1/4$ (Aarseth et al. 1974; Heggie & Mathieu 1986). Since the total energy E of the system is $E = K + W$ with $K = \frac{1}{2}\mathcal{M}_{\rm cl}\langle v^2\rangle$ being the total kinetic energy and $W = -(3\pi/32)G\mathcal{M}_{\rm cl}^2/R$ the potential energy of the Plummer sphere, we find from the virial theorem that

$$E = \frac{1}{2}W = -\frac{3\pi}{64}\frac{G\mathcal{M}_{\rm cl}^2}{R}. \tag{B1}$$

R is a quantity which determines the length-scale of a Plummer sphere. Using the specific definitions for G, $\mathcal{M}_{\rm cl}$, and E above, this scaling radius becomes $R = 3\pi/16$ in dimensionless units. The half-mass radius $r_{\rm h}$ can easily be evaluated by the formula (e.g. Spitzer 1987):

$$M(r) = \mathcal{M}_{\rm cl}\frac{r^3/R^3}{(1 + r^2/R^2)^{3/2}} \tag{B2}$$

when setting $M(r_{\rm h}) = \frac{1}{2}\mathcal{M}_{\rm cl}$. It yields $r_{\rm h} = (2^{2/3} - 1)^{-1/2}\, R = 1.30\,R$. The half-mass radius is located at the scalelength of $R = 0.766$, or about three-fourth of '*N*-body radii'.

The initial half-mass crossing time of a particle is

$$t_{\rm cr} = \frac{G\mathcal{M}_{\rm cl}^{5/2}}{(2E)^{3/2}}. \tag{B3}$$

Since the *N*-body-unit of time, $t_{\rm NB}$, is 1 when

$$t_{\rm NB} = \frac{G\mathcal{M}_{\rm cl}^{5/2}}{(-4E)^{3/2}}, \tag{B4}$$

immediately follows that $t_{\rm cr}/t_{\rm NB} = 2\sqrt{2}$.

In the situations considered here, the evolution of the cluster is driven by two-body relaxation. Therefore, a natural time-scale is the *half-mass relaxation time*. We use the definition of Spitzer (1987),

$$T_{\rm rh} = \frac{0.138N}{\ln\Lambda}\left(\frac{R_{1/2}^3}{G\mathcal{M}_{\rm cl}}\right)^{1/2}. \tag{B5}$$

For a Plummer model, the half-mass radius is $R_{1/2} = 1.305\,R$. $\mathcal{M}_{\rm cl}$ is the total stellar mass.

This paper has been typeset from a TEX/LATEX file prepared by the author.